Analytical and Bioanalytical Chemistry
https://doi.org/10.1007/s00216-024-05220-0

CRITICAL REVIEW

Application of gold nanoclusters in fluorescence sensing and biological detection

Kexin Tan[1] · Huizhen Ma[1,2] · Xiaoyu Mu[1] · Zhidong Wang[3] · Qi Wang[3] · Hao Wang[1] · Xiao-Dong Zhang[1,2]

Received: 29 November 2023 / Revised: 29 January 2024 / Accepted: 16 February 2024

Abstract

Gold nanoclusters (Au NCs) exhibit broad fluorescent spectra from visible to near-infrared regions and good enzyme-mimicking catalytic activities. Combined with excellent stability and exceptional biocompatibility, the Au NCs have been widely exploited in biomedicine such as biocatalysis and bioimaging. Especially, the long fluorescence lifetime and large Stokes shift attribute Au NCs to good probes for fluorescence sensing and biological detection. In this review, we systematically summarized the molecular structure and fluorescence properties of Au NCs and highlighted the advances in fluorescence sensing and biological detection. The Au NCs display high sensitivity and specificity in detecting iodine ions, metal ions, and reactive oxygen species, as well as certain diseases based on the fluorescence activities of Au NCs. We also proposed several points to improve the practicability and accelerate the clinical translation of the Au NCs.

Keywords Gold nanoclusters · Photoluminescence · Fluorescence sensing · Biological detection

Introduction

Metal nanoclusters consist of a few to several hundred metal atoms with ultra-small size (< 2 nm) and show unique physicochemical properties [1, 2], such as strong fluorescence, quantized charging, and discrete redox behavior [3]. Additionally, their properties can be tailored in a controllable manner, and thus [4, 5], metal nanoclusters were developed as nanozymes and fluorophores for use in a wide range of fields from sensing and catalysis, to biomedicine [6, 7].

In the past, researchers have developed various types of organic, inorganic, and composite materials with fluorescent properties, including single-walled carbon nanotubes (SWCNTs) [8], quantum dots (QDs) [9], rare-earth-doped nanoparticles (RE NPs) [10], semiconductor nanoparticles (SP NPs) [11], small-molecule dyes (SMDs) [12], and aggregation-induced illuminating aggregates (AIEgens) [13], which have greatly expanded the range of fluorophores available for biomedical applications. Inorganic nanomaterials show high quantum yield (QY) and strong resistance to photobleaching. However, low fluorescence QY (< 1%) and poor biocompatibility have limited their widespread use in bioimaging [9]. Water-soluble organic fluorophores with good biocompatibility generally suffer from low QY, poor photostability, and short emission wavelength [14]. Thereinto, the gold nanoclusters (Au NCs) have been developed rapidly due to their excellent properties such as good stability and biocompatibility [7, 15, 16]. The stability enables Au NCs to retain their structure and properties under different environmental conditions [17–19], rendering them more accessible

Published in the topical collection featuring *Nanozymes* with guest editors Vipul Bansal, Sudipta Seal, and Hui Wei.

Kexin Tan and Huizhen Ma have contributed equally to this work.

✉ Qi Wang
wqi619@126.com

✉ Hao Wang
hao_wang@tju.edu.cn

✉ Xiao-Dong Zhang
xiaodongzhang@tju.edu.cn

[1] Tianjin Key Laboratory of Brain Science and Neural Engineering, Academy of Medical Engineering and Translational Medicine, Tianjin University, Tianjin 300072, China

[2] Department of Physics and Tianjin Key Laboratory of Low Dimensional Materials Physics and Preparing Technology, School of Sciences, Tianjin University, Tianjin 300350, China

[3] Department of Radiobiology, Beijing Key Laboratory for Radiobiology, Beijing Institute of Radiation Medicine, Beijing, China

Published online: 04 March 2024

for synthesis and application in biomedicine [18, 20]. Au NCs exhibit molecular-like electron energy-level changes from quasi-continuous to discrete energy-level fluorescence behavior [21] and show strong enzyme-like catalytic activities and fluorescence performance [1, 22, 23]. Moreover, Au NCs display advantages due to their unique physiochemical properties [24], like high catalytic activities [25], low toxicity [26], large Stokes shift [27], and long fluorescence life [28]. Therefore, the Au NCs show promise in the fields of fluorescence sensing [29], bioimaging [30], catalytic detection, and environmental monitoring [25].

Au NCs show excellent performance on several enzyme mimics like glucose oxidase (Gox), peroxidase (POD), and catalase (CAT) [3, 31, 32] and are used for the detection and treatment of various diseases [33]. Especially, Au NCs attract more attention to their fluorescence for their good photostability [19], long Stokes shift [18], and emission in the near-infrared II (NIR-II) region which show great superiority in tissue penetration and high spatial–temporal resolution [34]. Therefore, Au NCs were explored as optical probes for bioimaging [35] and show prospects in a wide range of applications in fluorescence sensing and biological detection [15].

In addition to the fields of nanomedicine [36, 37], in vivo imaging [38, 39], cell labeling, and drug delivery [26], the biological detection usage of Au NCs and their complexes has attracted more attention [7, 40]. Here, we systematically summarized the molecular structure and fluorescence properties of Au NCs and highlighted the advances in fluorescence sensing and biological detection [41]. We focus on the detection of ions harmful to the living environment (such as Hg^{2+}, Cu^{2+}, CO^{3+}, Fe^{3+}, Pb^{2+}, CN^{-}, I^{-}, Cr^{3+}) and the detection of components or ions in organisms (such as glucose, hydrogen peroxide, phosphate, amino acids, various enzymes, and other proteins) [42].

Fluorescence properties of Au NCs

In the past decades, significant progress in Au NCs has been made in synthesis [43]. The structure and fluorescence properties of Au NCs are closely related to ligands [44], metal-to-metal interactions, and assembly methods. Stable ligands often play an important role in guiding their structures and properties. In addition to the commonly employed small mercaptan molecules as Au NC protection ligands [45], more ligands, such as proteins [46], can be easily further coupled, improving their application in biology and medicine [47]. In the synthesis of self-assembled nanoparticles [48], the collective interactions of the assembled components can be controlled to effectively endow new materials with special properties that enable them to have a wider range of applications [49].

Protein-stable Au NCs

Protein-stabilized gold nanomaterials are a unique class of biological nanomaterials with strong luminescence [47], which are suitable for chemical recognition in bioimaging and chemical sensing [46]. Protein molecules can be used as both stable ligands and structural directing agents to promote the formation of ultra-small Au NCs [50].

D. M. Chevrier et al. reported the stable luminescent Au NCs of bovine serum albumin by the one-pot self-reduction synthesis method (Fig. 1a) [49]. To identify the Au structure in Au bovine serum albumin (BSA), the extended X-ray absorption fine structure (EXAFS) was recorded, and the effective qualitative and quantitative analysis of the scattering characteristics was performed in the Fourier transform of EXAFS spectrum (FT-EXAFS). As illustrated in Fig. 1b, the FT-EXAFS of luminescent Au BSA with $Au_{25}(SR)_{18}$ and $Au_{38}(SR)_{24}$ were compared. The results revealed that most gold atoms are in the SR-Au-SR structure without a gold core structure, signifying that the gold atoms in Au BSA are most likely in the oxidation state of Au(I). In addition, an intermolecular gold affinity interaction between SR-Au(I)-SR structures in Au BSA can be obtained by analyzing the bond length [51]. Figure 1c displays the comparison of the experimental FT-EXAFS of Au BSA with the simulated spectra of all available Au(I)-SR nanoclusters ((rings ($Au_4(SR)_4$, $Au_5(SR)_5$, $Au_6(SR)_6$) and interlocked rings or catenanes ($Au_{10}(SR)_{10}$, $Au_{11}(SR)_{11}$, $Au_{12}(SR)_{12}$), and polymer ($[Au(SR)]_x$)). It can be found that the scattering characteristics of the $Au_{10}(SR)_{10}$ alkane structure (two interlocked $Au_5(SR)_5$ rings) closely resemble those of the four positions immediately following the Au-S peak [52]. Moreover, the interaction distance between them shows a remarkable similarity. According to the number of Au atoms of each BSA and the main Au-S structure environment determined by EXAFS, there may be two $Au_{10}(SR)_{10}$ alkane structures in each BSA molecule. The additional 1–3 gold atoms can be attributed to the small amount of $Au(SR)_2$ monomer formed in BSA. TOA^{+}/toluene phase transfer experiment was carried out with $Au_{10}(SG)_{10}$ to simulate the protection and hardening environment of protein and verify the emission characteristics of Au BSA nanoclusters containing $Au_{10}(SG)_{10}$. The photoluminescence (PL) intensity of Au(I)-SR cluster in a nonrigid BSA molecule is decreased by about 5 times with a maximum emission redshift of 15 nm (Fig. 1d). However, the luminescence of rigid $Au_{10}(SG)_{10}$ is enhanced more than 10 times (QY = 5.0%) with the blue shift of 15 nm (Fig. 1e), which is consistent with the 15 nm red shift in the opposite direction of the above Au BSA (Fig. 1d), further verifying the similar stiffening effect on Au(I)-SR nanoclusters [53]. In addition, the average PL decay life of rigid $Au_{10}(SG)_{10}$ also almost

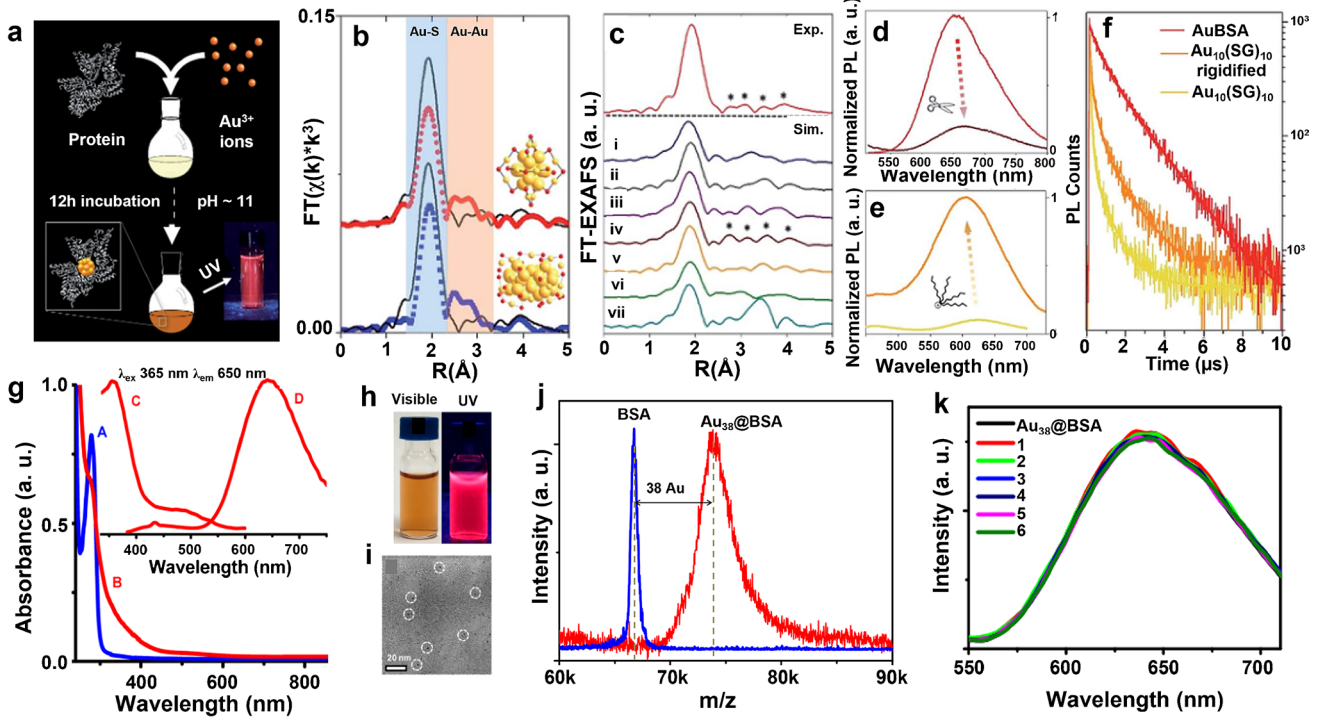

Fig. 1 Physical properties of protein-stabilized Au NCs. **a** Method for synthesizing Au NCs from protein (bovine serum albumin). **b** Au L_3-edge FT-EXAFS of luminescent Au BSA (black line) with $Au_{25}(SR)_{18}$ (red dot) and $Au_{38}(SR)_{24}$ (blue dot) (inset, respective models with Au (yellow) and S (red) atoms). **c** Simulated Au L_3-edge FT-EXAFS of Au(I)-SR structures. **d** Resultant luminescence decrease of Au BSA nanoclusters (un-rigidified, dark red line) and **e** luminescence enhancement of $Au_{10}(SG)_{10}$ nanoclusters (rigidified, orange line). **f** Photoluminescence decay lifetime traces of Au BSA nanoclusters (red), rigidified $Au_{10}(SG)_{10}$ nanoclusters (orange), and original $Au_{10}(SG)_{10}$ nanoclusters (yellow) [49] (published with permission from Chevrier et al. (2018), ©2018 The Royal Society of Chemistry). **g** Comparison of UV-Vis spectra for (A) pure BSA and (B) Au_{38}@BSA. PL (C) excitation and (D) emission spectra of the cluster. **h** The photograph of cluster solution under visible and UV light. **i** HRTEM image of the cluster. **j** Comparison between MALDI MS of BSA and Au_{38}@BSA. **k** The PL emission spectra of Au_{38}@BSA [46] (published with permission from Mohanty et al. (2019), ©2019 American Chemical Society)

doubled (from 0.120 to 0.210 ms) (Fig. 1f). In general, the rigidity of $Au_{10}(SG)_{10}$ and the nonrigidity of Au(I)-SR nanoclusters in Au BSA exhibit the similar luminescence properties in the two systems, which further connects the luminescence properties of small mercaptan-stabilized Au NCs and the protein-stabilized Au NCs.

The visible absorption spectrum, PL excitation spectrum, and emission spectrum of Au BSA are shown in Fig. 1g [46]. The decrease in absorption intensity of Au BSA is observed at 280 nm and a shoulder at 375 nm without obvious absorption characteristics, and the Au NCs have excitation maxima at 365 nm and 500 nm. Under the excitation of 365 nm, the Au NCs exhibit two emission peaks. One is located around 450 nm, attributed to the weak luminescence of the protein, while the other is at 645 nm, arising from the emission of cluster [54]. For example, Fig. 1h shows the picture of the Au NCs under visible and ultraviolet light, and the Au NCs emit red light in ultraviolet light. According to the high-resolution transmission electron microscopy (HRTEM) analysis in Fig. 1i, it can be found that the core of the Au NCs is only below 2 nm. Matrix-assisted laser desorption ionization mass spectrometry (MALDI MS) indicates that the number of gold atoms in the core of the cluster is 38, and the Au NCs is Au_{38}BSA with atomic precision (Fig. 1j) [46]. Moreover, no enhancement of emission intensity over time is observed in the experimental group in the controlled PL study, indicating the excellent stability of Au_{38}BSA (Fig. 1k). Therefore, protein-stabilized gold nanomaterials suitable for bioimaging and chemical sensing have wide applications.

Sulfide-stable Au NCs

The high stability and accessibility of polynuclear gold(I)–chalcogenide complexes enable them to be used as model compounds of cluster species in various fields, including catalysis [55], bionics [45], nano-aggregates [56], luminescence research, chemical sensing [57], structure conversion, and chirality. Polynuclear gold(I)–chalcogenide complexes are endowed with a variety of configurations and structure-dependent photophysical properties based on the

gold affinity interaction. These Au NCs exhibit fluorescent properties with emission ranges in the visible region, demonstrating good prospects for applications in bioimaging.

For example, the solid-state structures of three different polynuclear gold(I)–chalcogenide complexes of $L^HAu_{10}S_4$-Cl, $[Au_{14}(\mu_3\text{-}S)_6(\mu\text{-bdppmapy})_5]^{2+}$, and $[Au_{18}(\mu_3\text{-}S)_9(\mu\text{-bdppmapy})_6]^{2+}$ were further determined by single-crystal X-ray diffraction (SCXRD) (Fig. 2a–c). $L^HAu_{10}S_4$-Cl crystallizes in a monoclinic $p2_1/n$ space group, which is similar to propeller-shaped decanuclear gold(I) four diphosphine ligand coordinates with eight gold(I) centers in a large cycle, and the other two gold(I) centers are located in the central part through Au-S coordination bond due to the interaction between Au (I)···Au (I) and Au···Au (I) (Fig. 2a) [58]. $[Au_{14}(\mu_3\text{-}S)_6(\mu\text{-bdppmapy})_5]^{2+}$ crystallizes in the P1 space group of the triclinic system; among them, $[Au_{14}S_6(bdppmapy)_5]^{2+}$ is composed of $Au_6S_2(bdppmap)$ unit and $Au_8S_4(bdppmap)_4$ unit, which is interconnected by Au-S and metallophilic interaction (Fig. 2b) [59]. $[Au_{18}(\mu_3\text{-}S)_9(\mu\text{-bdppmapy})_6]^{2+}$ in triangle R3 and the $[Au_{18}S_8(bdppmapy)_6]^{2+}$ is composed of two $Au_9S_4(bdppmap)_3$ units interconnected by Au-S and eosinophilia interactions (Fig. 2c) [59].

The ultraviolet-visible (UV-Vis) of $L^HAu_{10}S_4$-Cl crystal in dimethyl sulfoxide (DMSO) exhibits the absorption maximum and shoulder at 336 and 410 nm, respectively (Fig. 2d) [60]. The solid-state emission spectrum of $L^HAu_{10}S_4$-Cl at ambient temperature is illustrated in Fig. 2d, exhibiting double-emission behavior with the maximum emission value observed in the green (515 nm, $\tau = 4.3$ μs) and red (675 nm, $\tau = 5.4$ μs) regions, which are tentatively designated as metal-perturbed intraligand phosphorescence and the triplet ligand-to-metal-metal charge-transfer transitions, respectively [61]. The UV-Vis absorption spectrum reveals that $[Au_{14}(\mu_3\text{-}S)_6(\mu\text{-bdppmapy})_5]^{2+}$ has absorption peaks at 320 nm and 365 nm, while $[Au_{18}(\mu_3\text{-}S)_9(\mu\text{-bdppmapy})_6]^{2+}$ exhibits absorption peaks at 320 nm, 395 nm, and 440 nm (Fig. 2e). In addition, the two Au NCs display excellent stability in the air and emit bright yellow–green light in the solid-state ($[Au_{14}(\mu_3\text{-}S)_6(\mu\text{-bdppmapy})_5]^{2+}$ $\lambda_{em} = 540$ nm; $[Au_{18}(\mu_3\text{-}S)_9(\mu\text{-bdppmapy})_6]^{2+}$ $\lambda_{em} = 518$ nm) with the QYs of

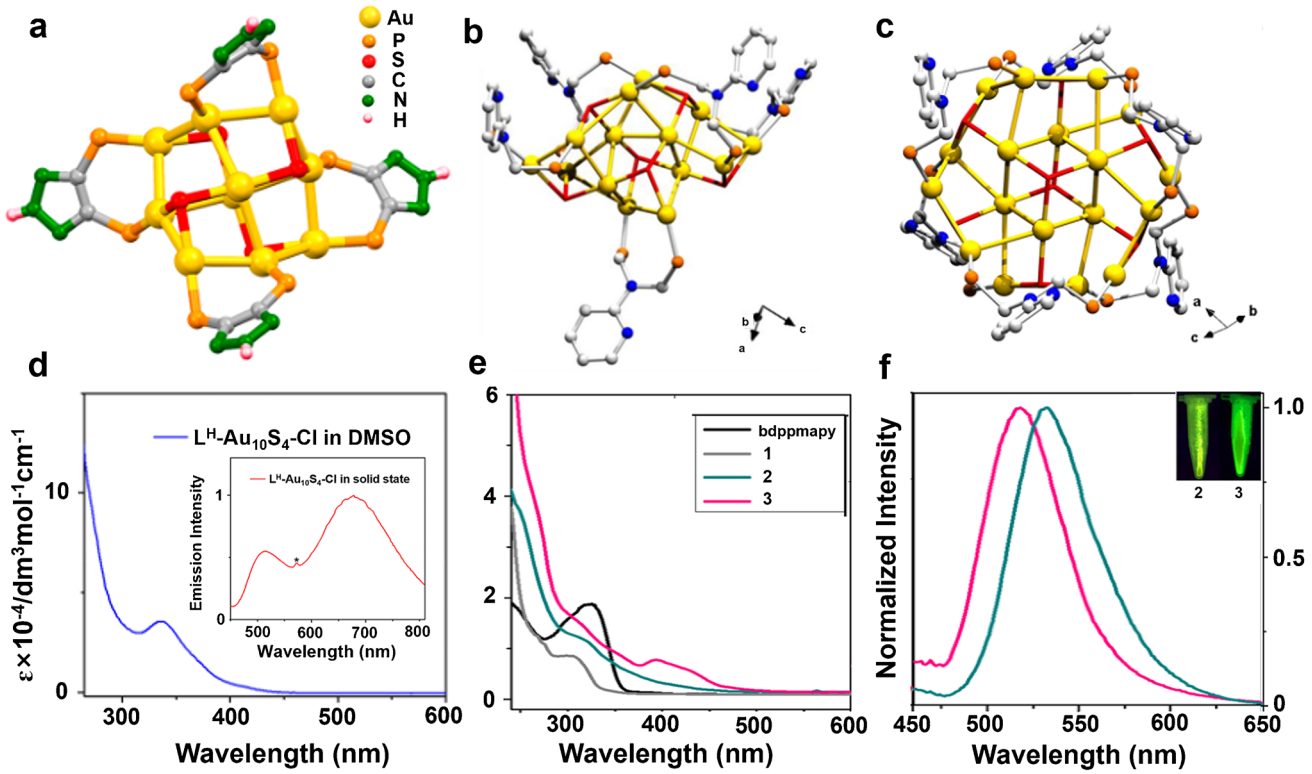

Fig. 2 Physical properties of sulfide-stabilized Au NCs. Crystal structures of **a** L^H-$Au_{10}S_4$-Cl [58] (published with permission from Yao et al. (2021), ©2021 American Chemical Society), **b** $[Au_{14}(\mu_3\text{-}S)_6(\mu\text{-bdppmapy})_5]^{2+}$ and **c** $[Au_{18}(\mu_3\text{-}S)_9(\mu\text{-bdppmapy})_6]^{2+}$ [59] (published with permission from Liu et al. (2019), ©2019 American Chemical Society). Color legend: yellow, Au; red, S; orange, P; gray, C; green or blue, N. Phenyl rings and hydrogen atoms have been omitted. **d** UV-vis spectrum in DMSO [58] (published with permission from Yao et al. (2021), ©2021 American Chemical Society). **e** UV-vis absorption spectra of bdppmapy and $[(AuCl)_2bdppmapy]$ (1), $[Au_{14}(\mu_3\text{-}S)_6(\mu\text{-bdppmapy})_5]^{2+}$ (2), and $[Au_{18}(\mu_3\text{-}S)_9(\mu\text{-bdppmapy})_6]^{2+}$ (3) in CH_2Cl_2, and (**f**) emission spectra of (2) and (3) in the solid state [59] (published with permission from Liu et al. (2019), ©2019 American Chemical Society)

20.7% and 26.6% at room temperature, respectively (Fig. 2f) [62]. The aforementioned properties demonstrate the favorable photoluminescent characteristics of diverse structures of polynuclear gold(I)–chalcogenide complexes, rendering them promising probe for fluorescence sensing and biological monitoring.

Self-assembled Au NCs

The self-assembly of Au NCs into an ordered hierarchical structure represents a highly effective strategy for tailoring the properties of molecular-like materials [63] and has gained increasing recognition in diverse fields such as biomedicine, green catalysis [49], and clean energy [64]. Moreover, recent studies have demonstrated that the luminescence of Au NCs can be enhanced by the effective gold affinity interaction between Au NCs based on this self-assembled tight arrangement and ordered Au NCs [65].

For instance, Fig. 3a schematically illustrates the evolution of the self-assembly from the initial $[Au_{25}(SR)_{18}]$ NCs to well-defined nanoribbons [66]. Under cyclic dialysis conditions, the maternal $[Au_{25}(P\text{-}MBA)_{18}]$ NCs undergo controlled instability, leading to a transformation in the surface motif of Au NCs from the original SR-[Au(I) SR]$_2$ motifs to a longer SR-[Au(I) SR]$_x$ motif ($x > 2$), resulting in smaller NCs. The formed smaller NCs exhibit the characteristic structure of a small Au_0 core covered by a compact long SR-[Au(I) SR]$_x$ motif ($x > 2$). Due to the abundance of adjacent

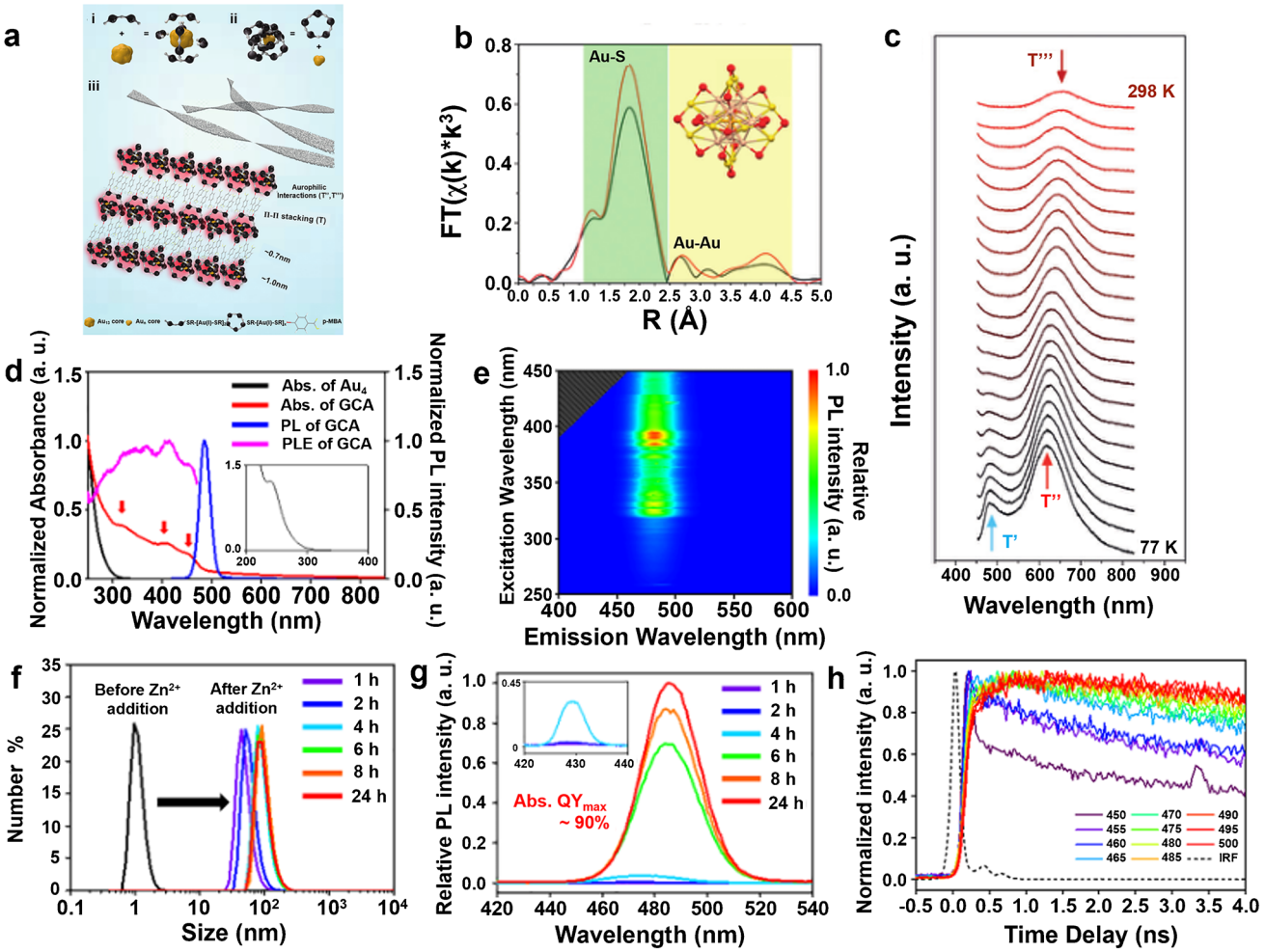

Fig. 3 Physical properties of self-assembled Au NCs. **a** Schematic illustration of self-assembly evolution from the original $[Au_{25}(SR)_{18}]$ NCs into well-defined nanoribbons. **b** Au L_3-edge FT-EXAFS spectrum of $[Au_{25}(p\text{-}MBA)_{18}]$ NCs (black line) and the as-assembled nanoribbons (red line). **c** The variation of emission spectra of nanoribbons excited at 365 nm from 77 to 298 K [66] (published with permission from Wu et al. (2019), ©2019 Wiley-VCH Verlag GmbH & Co. KGaA, Weinheim). **d** Change of absorption spectra before (black) and after Zn^{2+} ion addition (red) and PL (blue, $\lambda_{ex} = 410$ nm), and PLE of GCA (magenta, $\lambda_{em} = 485$ nm). **e** Excitation–emission contour mapping of GCA. **f** DLS and **g** PL showing the gradual formation of GCA by the addition of Zn^{2+} ions. Inset of **g**: zoom in PL spectra for 1, 2, and 4 h. **h** Time-resolve PL spectra of GCA depending on the emission wavelength as indicated [69] (published with permission from Chang et al. (2021), ©2021 American Chemical Society)

components on the Au(I) surface [67], NCs induce strong metallophilic interaction to form closely aligned nanowires. In the FT-EXAFS spectrum of the Au L_3 edge (Fig. 3b), the positions corresponding to Au-S and Au-Au are depicted in green and yellow, respectively. The peaks of the centers of Au-S, Aucenter-Auapex, Auapex-Auapex, Auapex-Austaple, and Austaple-Austaple bonds are observed at approximately 1.83, 2.64, 3.12, 3.59, and 4.11 Å, respectively [68]. Among them, Adcenter, Auapex, and Austaple refer to the central Au atoms, which are located at the apex of the icosahedral Au_{13} nucleus and in the SR-[Au(I) SR]$_2$ staple motif, respectively. The most prominent spectral change after self-assembly is attributed to the significant increase in protein content. The Au-S and Austaple-Austaple characteristics provide support for the formation of the long SR-[Au(I) SR]$_x$ motif ($x > 2$), which is consistent with the description in Fig. 3a. Hogan Chang et al. successfully synthesized self-assembled $Au_4(MHA)_4$ nanoclusters through the interaction between anionic carboxylic acid groups in MHA ligands and Zn^{2+} ions in a cross-linking manner [69]. The absorption spectrum of the Au NCs displays three wide peaks at 327, 410, and 455 nm, which is attributed to the discrete electronic structure of the gold cluster assembly (GCA) (Fig. 3d, red line) with a characteristic surface plasmon resonance peak around 520 nm. It is worth noting that the blue–green emission of GCA is emitted at 485 nm under UV irradiation (Fig. 3d, blue line). The half-maximum width of the peak (~25 nm) indicates the high optical purity of GCA. The consistency between PL excitation (PLE) and absorption confirms that the blue emission originates from GCA itself (Fig. 3d, magenta line) [55]. In addition, we confirm that the fluorescence originates from a single emitting species by analyzing the excitation–emission contour map of GCA, which demonstrates the obvious independence of excitation and emission wavelengths (Fig. 3e). This characteristic minimizes any potential influence of excitation wavelength on emission wavelength [70]. As shown in Fig. 3f and g, an increase in intensity was observed when the average size of GCA analyzed by dynamic light scattering (DLS) increased, and even GCA of the same size showed stronger emission after a long aging time. At a range of 450–460 nm, GCA showed PL dynamics associated with its emission wavelength. While the main fluorescence was enhanced, an instantaneous attenuation of 70 ps was observed at the blue edge wavelength (Fig. 3e) [71]. In addition, self-assembled gold nanoclusters also exhibit temperature sensitivity characteristics. In self-assembled nanoribbons, T′ emission (Fig. 3c) decreased with the increase of temperature; however, T″ emission remains in the nanoribbons, but gradually shifted to 655 nm (T‴ state) at room temperature [72]. This slight red shift indicates an affinity interaction between Au NCs and their environment that is sensitive. Based on these properties elucidated above, self-assembled Au NCs possess excellent PL and temperature sensing properties and can be used as high-efficiency luminescent biomarkers for fluorescence sensing and biological monitoring.

Fluorescence sensing and biological detection based on Au NCs

The strong PL, excellent photostability, favorable biocompatibility [73], and low toxicity of Au NCs have attracted extensive research attention in the fields of fluorescence sensing and bioimaging [74], including the detection of ions or metal ions harmful to the natural living environment (such as Hg^{2+}, Ag^{+}, Cu^{2+}, Co^{3+}, Fe^{3+}, Pb^{2+}, CN^{-}, I^{-}, Cr^{3+}, H_2S) [75–77], as well as molecules or ions in organisms (such as glucose, hydrogen peroxide [78], phosphate, amino acids [79], and various enzymes [80] and other proteins [81]).

Quantitative detection of nonmetal ions

Nonmetal ions play an important role in environmental impacts and various physiological and pathological processes within living organisms. Iodide(I^{-}) plays an important role in some human physiological activities, including intellectual development [77] and basic metabolism [82]. Iodine deficiency and excessive intake may induce a variety of diseases [83]. Cyanide one of the most potent toxins in the environment is acutely hazardous to mammals and aquatic organisms by inactivating cytochrome C oxidase and inhibiting oxygen transport [84]. Many countries and organizations have established guidelines and standards for cyanide levels in drinking water [85]. Hydrogen sulfide (H_2S) also plays an important role in numerous physiological and pathological processes within living organisms, including angiogenesis, vasodilation, inflammation, apoptosis, and oxygen sensing [86]. Dysregulated levels of H_2S may be associated with serious disorders, such as Down's syndrome [87], Alzheimer's disease, diabetes mellitus, and decompensated cirrhosis [88]. Therefore, the development of sensitive and reliable methods for nonmetal ion detection holds great importance in living systems [89].

Jiang et al. developed a simple colorimetric fluorescent nanosensor based on carbon dots (CDs)/Au NCs for sensitive quantitative detection of I^{-} (Fig. 4) [90]. CDs and Au NCs were mixed in a certain proportion to form a colorimetric fluorescence probe solution. Figure 4a shows the dependence of the fluorescent intensity of the probe on I^{-} concentration. The PL intensity increases with the increase of I^{-} concentration. Correspondingly, the fluorescent color changes from green to yellow and then to orange with the increase of I^{-} concentration. The relationship between PL intensity and I^{-} concentration was quantitatively evaluated by plotting the linear relationship between I_{600}/I_{486} ratio and

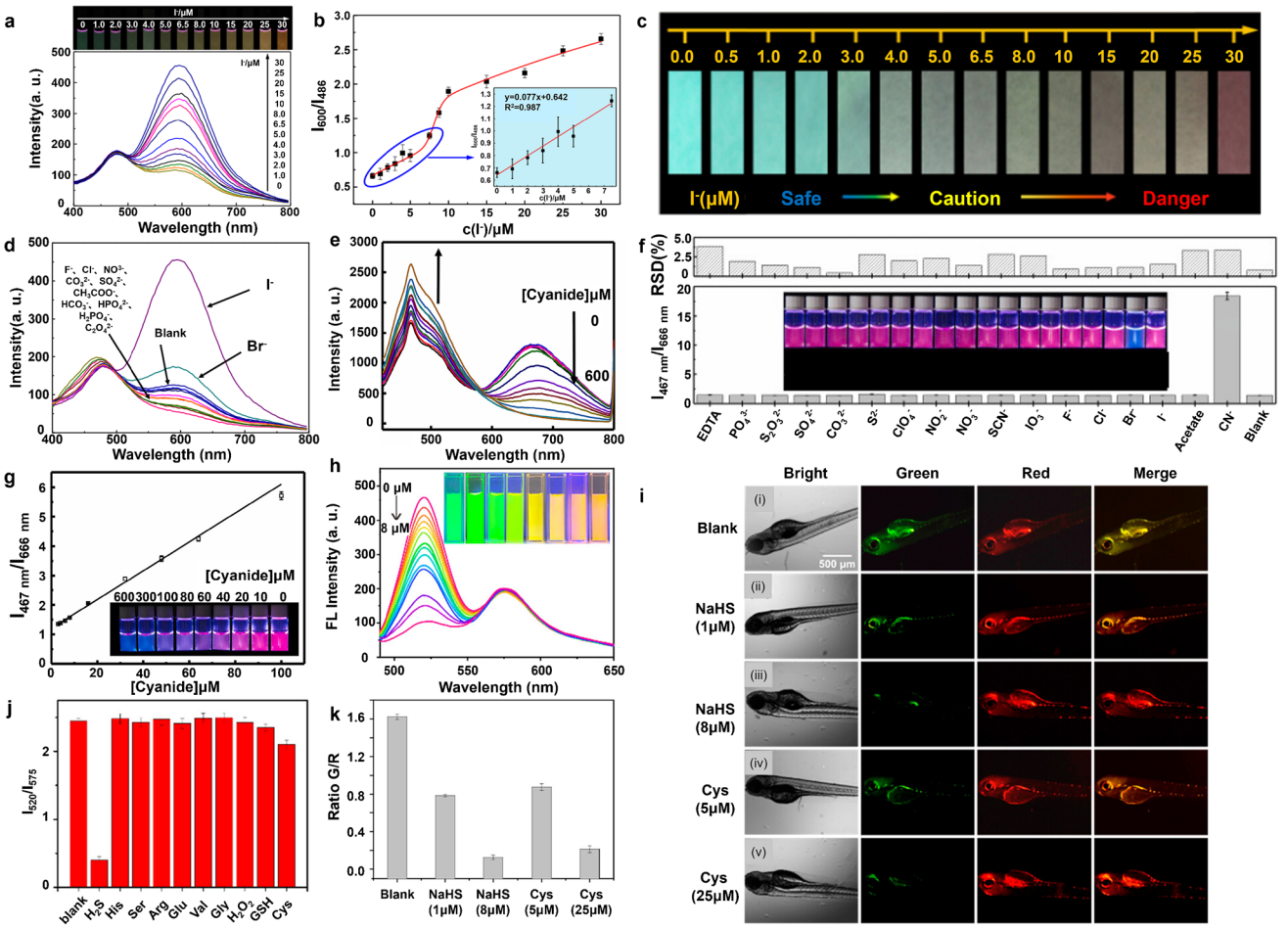

Fig.4 Au NCs for the quantitative detection of nonmetal. **a** FL spectra of the colorimetric fluorescent probe with the addition of I^- (the initial FL intensities of Au NCs and CDs were adjusted to a ratio of 3.5/1). The inset shows the corresponding fluorescence photo under a 365 nm UV lamp. **b** Plotting the I_{600}/I_{486} ratio vs the concentrations of I^-. **c** Visual detections of iodide ions in urine. The photos were taken under a 365 nm UV lamp. **d** The colorimetric fluorescent responses to various inorganic anions [90] (published with permission from Jiang et al. (2021), ©2021 American Chemical Society). **e** Fluorescence spectra (λ_{ex} = 380 nm) of the LysNP-Au NCs as a function of the cyanide concentration. The arrow indicates the signal changes with increasing the cyanide concentration, 3, 4, 6, 8, 16, 32, 48, 64, 100, 200, 400, and 600 μM. **f** Effect of different metal ions (300 μM) on the I_{467} nm/I_{666} nm value of the LysNP-Au NCs. **g** A plot of the I_{467} nm/I_{666} nm value versus the cyanide concentration. Inset in **g**: digital photos of the LysNP-Au NCs in the presence of increasing cyanide concentration [95] (published with permission from Tseng et al. (2021), ©2021 Elsevier Inc. All rights reserved). **h** Fluorescence spectral responses of RBDA to H_2S with varying concentrations from 0 to 8 μM under the excitation wavelength of 470 nm. (Insets) The corresponding sample solutions under UV light irradiation. **i** Fluorescence imaging of exogenous and endogenous H_2S in zebrafish. **j** Ratiometric fluorescence responses of the probe to H_2S and other coexistence species with the concentration of 8 μM. **k** The relative fluorescence intensity ratio data in **i** [99] (published with permission from Xiang et al. (2023), ©2023 American Chemical Society)

I^- concentration (Fig. 4b) [91]. Figure 4d displays the colorimetric fluorescence reaction of the fluorescent probe to common different interfering anions (F^-, Cl^-, Br^-, NO^{3-}, CO_3^{2-}, SO_4^{2-}, CH_3COO^-, HCO_3^-, HPO_4^{2-}, $H_2PO_4^-$, and $C_2O_4^{2-}$). A single inorganic anion did not demonstrate the capacity to induce a notable alteration in the fluorescence intensity ratio (I_{600}/I_{486}) of the probe [92]. These experiments reveal the good selectivity of CDs/Au NC fluorescent probes. Through inkjet printing technology, the well-dispersed colorimetric fluorescent probe solution is fixed on the filter paper to make a fluorescent paper strip for the visualization of iodine ion detection. Under the excitation of a 365-nm ultraviolet lamp, the paper sensor exhibits a highly uniform green luminescence [93]. Upon addition of iodine ion solution, the obvious fluorescence color change can be observed by the naked eye. In addition, when different concentrations of I^- solution are dropped on the fluorescent paper strip, the fluorescence color of the paper sensor gradually changes from green to yellow and finally turns orange with the increase of iodine ion concentration (Fig. 4c). The detection range of iodine

ion solution concentration extends approximately from 0 to 30 μM [94]. Compared with other probes, CDs/Au NC fluorescent probes exhibit a suitable limit of detection (LOD), a wider detection range, and a more prominent visual detection effect. Furthermore, CDs/Au NC fluorescent probes can be fabricated into a simple fluorescent detector to analyze I^- intuitively and conveniently in a real-time or on-site environment and facilitate health screening in time.

Zeng et al. developed a strategy to fabricate lysozyme nanoparticle-encapsulated gold nanoclusters (LysNP-Au NCs) as dual-emission probes for ratiometric sensing of cyanide by fluorescence resonance energy transfer (FRET) [95]. Upon varying the cyanide concentration was varied in the range of 0 ~ 600 μM, the fluorescence intensity of lysozyme nanoparticles exhibits a gradual increase at 467 nm and a corresponding decrease at 666 nm within the LysNP-Au NCs (Fig. 4e). The I_{467} nm/I_{666} nm values of LysNP-Au NCs exhibited linear variation ($R^2 = 0.9957$) over the cyanide concentration range of 3 ~ 100 μM (Fig. 4g) [96]. The relative standard deviations (RSDs) of the I_{467} nm/I_{666} nm values obtained at each cyanide concentration were less than 2.7% ($n = 3$), indicating excellent reproducibility provided by LysNP-Au NCs for the quantitative analysis of cyanide. Moreover, the LysNP-Au NC concentration could detect concentrations as low as 10 μM even with naked eye observation (Fig. 4g), which is close to the maximum allowable level of cyanide in drinking water set by the US Environmental Protection Agency [97]. Subsequently, the selectivity of LysNP-Au NCs for cyanide over potentially interfering anions was evaluated. Only cyanide induced significant changes in the I_{467} nm/I_{666} nm values, demonstrating the high selectivity of LysNP-Au NCs (Fig. 4f). The excellent selectivity offered by LysNP-Au NCs for cyanide may be due to the strong binding of lysozyme to the gold surface, which inhibits the corrosion of Au NCs by iodide, sulfide, and thiosulfate [98]. The results indicate the great potential of LysNP-Au NCs as a proportional probe for the determination of cyanide ions in composite matrices.

A novel ratiometric fluorescent probe (RBDA) was designed by Xiang et al. for sensing the H_2S based on the fluorescence resonance energy transfer (FRET) induced by electrostatic attraction between Au NCs and rhodamine B [99]. The detection performance of the prepared probes was explored through quantitative analysis. The fluorescence intensity of the RBDA solution was measured after the adding different concentrations of H_2S. As shown in Fig. 4h, the fluorescence peak at 520 nm gradually decreased with the increase of H_2S concentration n from 0 μM to 8 μM, while the fluorescence peak at 575 nm remained unchanged [100], demonstrating a proportional fluorescence response to H_2S. Unlike the individual Au NCs and rhodamine B with FRET effect, the decrease of the emission peak at 520 nm had no effect on the peak at 575 nm due to the slight change of the surface structure of the RBDA probe after assembly. A gradual emission color change from green to yellow to orange could be observed in the corresponding sample solution under UV light (inset in Fig. 4h) [101]. As shown in Fig. 4j, negligible changes were observed in fluorescence ratio in the presence of various biomolecules such as His, Ser, Arg, Glu, Val, Gly, H_2O_2, Cys, and GSH. However, I_{520}/I_{575} significantly reduced the presence of H_2S, indicating the high specificity of this probe toward detecting H_2S presence. Consequently, a novel H_2S proportional fluorescent probe with high sensitivity and selectivity was developed [102]. To further investigate its imaging capability in vivo, zebrafish larvae were chosen as a model for sensing exogenous and endogenous H_2S. RBDA was incubated with zebrafish for 2 h. Green and red fluorescence could be clearly observed (Fig. 4i), suggesting good tissue penetration and potential for in vivo imaging [103]. The changes in exogenous H_2S levels in zebrafish were monitored by treating them with different concentrations of NaHS (1 μM and 8 μM). It was observed that the green fluorescence of zebrafish treated with both probe and NaHS significantly decreased compared to those treated with probe alone. The reduction in fluorescence intensity exhibited a positive correlation with the concentration of NaHS [104]. Subsequently, endogenous H_2S levels were assessed by incubating zebrafish with Cys to stimulate H_2S production. As the concentration of Cys increased (5 μM and 25 μM), a concentration-dependent decrease in green fluorescence was observed, while the red fluorescence remained relatively unchanged [105]. The relative quantitative intensity data provided a more intuitive visualization of proportional fluorescence changes (Fig. 4k). These results demonstrate the ability of the designed RBDA nanoprobes for quantification of H_2S levels in vivo.

By analyzing the above properties, the CDs/Au NC fluorescent probe exhibits a suitable detection limit and wider detection range for iodide ions. The LysNP-Au NCs enable ratiometric fluorescence sensing of 3–100 μM cyanide in tap water, and the fluorescent nanoprobe RBDA based on Au NCs has good dual-emission fluorescence properties with a direct, fast, highly sensitive and selective proportional fluorescence response to H_2S [106]. Therefore, the gold nanoprobe can be utilized for the rapid and sensitive detection of nonmetallic ions, providing a novel analytical platform for their selective identification.

Quantitative detection of metal ions

Heavy metal pollution is a global problem, which harms the environment and poses a serious medical threat to human health [107]. Many heavy metal ions are known to be toxic or carcinogenic due to their inability to biodegrade and propensity to accumulate within organisms. Mercury ion (Hg^{2+}), for instance, is a highly toxic and widely distributed

heavy metal pollutant that accumulates in organisms [108], inducing significant harm to the brain [109], nervous system [110], endocrine system [111], and even kidney [112], which represents a severe threat to human health and the natural environment [113]. Silver ions, which are extensively used in electronics [76], photography, pharmaceuticals, and other industries [114], are also released into the environment in substantial quantities through waste and emissions every year. Simultaneously, Ag^+ can inactivate sulfhydryl enzyme [115]; combine with amine, imidazole, and carboxyl groups of various metabolites; and replace essential metal ions such as Ca^{2+} and Zn^{2+} in hydroxyapatite in bone [116], causing significant harm to organisms. Although copper is an essential trace element, its improper application may lead to toxic reactions due to copper metabolism disorders, resulting in the deposition of this element in the liver, brain, and other tissues. Excess copper in the body can cause hepatomegaly and other diseases. Therefore, the development of simple methods to selectively and sensitively determine heavy metal ions is undoubtedly an important step in environmental and health monitoring [117].

Zhang et al. reported a bifunctional, rapid, ultra-sensitive, and label-free fluorescent sensor based on cytidine-stabilized Au NCs for the detection of Ag^+ and Hg^{2+} [118]. As depicted in Fig. 5a, the emission spectrum of Au NCs excited at 370 nm shows an emission peak at approximately 490 nm, which is attributed to the in-band transition of free electrons in Au NCs. Concurrently, it was observed that AuAg NCs exhibited strong yellow fluorescence under 365 nm ultraviolet light (Fig. 5a) with the emission spectrum red-shifted from 490 to 560 nm, and the fluorescence of Au NCs was enhanced [119]. In addition, the addition of 0.1 mm Hg^{2+} to AuAg NCs resulted in a significant reduction of the emission intensity of the system, and very weak fluorescence was observed under 365 nm ultraviolet light (inset of Fig. 5a). Importantly, the correlation process between the enhancement of Au NC fluorescence by Ag^+ and the quenching of AuAg NCs fluorescence by Hg^{2+} is very rapid with the fluorescence reaching a constant value within 5 s (Fig. 5b) [120]. This demonstrates that cytidine-stable Au NCs and AuAg NCs possess excellent fluorescence properties for the detection of Ag^+ and Hg^{2+}. The results depicted in Fig. 5a and d show that in the presence of Ag^+ and other metal ions (the concentration is 7.5 times higher than Ag^+), the relative fluorescence intensity of Au NCs, excluding Ag^+, has no significant effect on the fluorescence intensity of Au NCs [121]. The above results show that Au NCs possess high sensitivity and specificity for Ag^+, rendering them a suitable candidate for the biological monitoring of Ag^+. In addition, the fluorescence response to the other 12 essential metal ions at 100 mM concentration was further investigated (Fig. 5e, f). It was observed that only Hg^{2+} could significantly reduce the fluorescence, and other metal ions would not interfere with the detection of Hg^{2+} [122]. The results indicate that AuAg NCs exhibit excellent dispersion and high selectivity in aqueous solution, making them suitable for the sensitive detection of Hg^{2+} in a practical sample system.

Furthermore, Saleh et al. proposed a novel strategy for the synthesis of highly luminescent Au NCs based on coffee Arabica seed extract (CASE) combined with ethylene diamine tetraacetic acid (EDTA) and sodium borohydride as a masking agent to improve the selectivity of Au NCs toward Cu^{2+} and Hg^{2+} ions [117]. $NaBH_4$ possesses the ability to reduce Hg^{2+} but lacks the capability to reduce weaker oxidizing properties such as Cu^{2+}, Mg^{2+}, and Ba^{2+}. Consequently, it can be utilized as a discerning masking agent for Hg^{2+} ions. As illustrated in Fig. 5g, the fluorescence intensity of CASE-Au NCs decreased with the increase of Cu^{2+} ion concentration in a mixed solution containing 100 μM $NaBH_4$, 12 μM Hg^{2+} ion, 20 mM phosphate buffer at pH 7.4, and CASE-Au NC solution [123]. The Stern Volmer equation was employed to construct a plot of relative intensity (F_o/F) versus Cu^{2+} concentration, as shown in Fig. 5h. A linear relationship was acquired in the concentration range of 0 ~ 7 μM with a correlation coefficient of $R^2 = 0.9988$. The LOD was calculated to be 14.78 nM assuming an accuracy of ± 1% for the quantification of fluorescence intensity. EDTA served as a masking agent for the Cu^{2+} and Hg^{2+} also demonstrated a high binding affinity for EDTA. The logarithm of the Hg(II)-EDTA formation constant was 21.7, but the complex formed did not change the oxidation state of the mercury ion Hg^{2+}, and it also had the effect of binding to Au(I) and CASE-Au NC fluorescence burst [124]. As shown in Fig. 5i, the fluorescence intensity of CASE-Au NCs decreased during the excess addition of Hg^{2+} in a mixed solution containing 7 μM Cu^{2+}, 50 μM EDTA, 20 mM phosphate buffer at pH 7.4, and CASE-Au NC solution. Utilizing the Stern Volmer equation, the relative intensity (F_o/F) was plotted versus Hg^{2+} concentration (Fig. 5j) [125]. A linear relationship was observed within the concentration range of 0 ~ 14 μM with a correlation coefficient of $R^2 = 0.9992$. The LOD was estimated to be 35.21 nM, assuming that the fluorescence intensity was measured with an accuracy of ± 1%.

Based on the analysis of the aforementioned properties, Au NCs and AuAg NCs demonstrate a significant rapid response and high selectivity to Ag^+ and Hg^{2+} with the detection concentrations of Ag^+ and Hg^{2+} at 10 and 30 nm, respectively [126]. In addition, CASE-Au NCs were effective in detecting Cu^{2+} and Hg^{2+} cations in the presence of masking agents. Therefore, Au NCs can be used as a new analytical platform for the rapid and selective detection of Ag^+, Hg^{2+}, and Cu^{2+}.

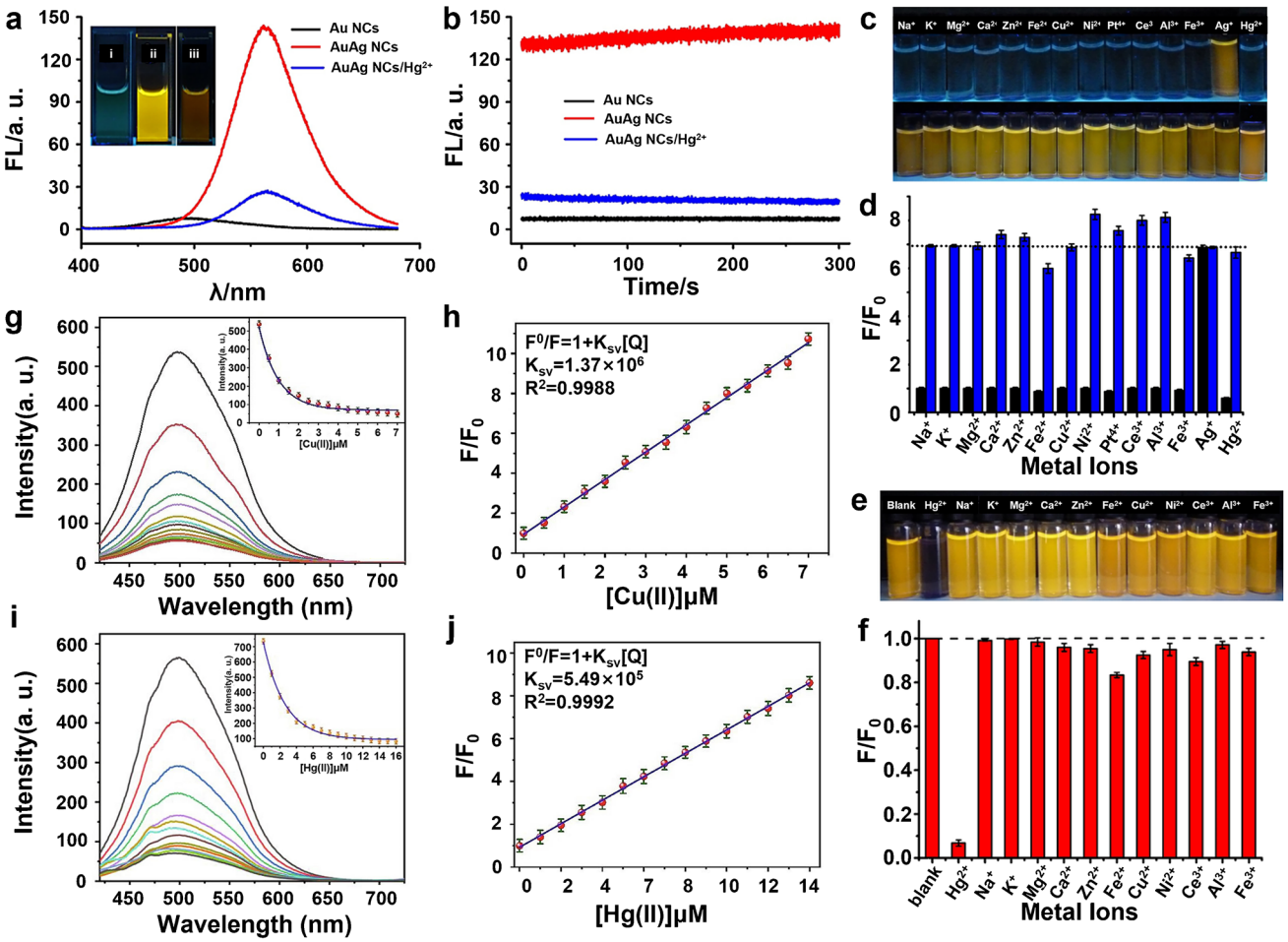

Fig. 5 Au NCs for the quantitative detection of metal ions. **a** The fluorescence emission spectra (λ_{ex} = 370 nm) of the as-prepared cytidine-stabilized Au NCs in black line and upon addition of 10 Mm Ag^+ (red line) and 0.1 Mm Hg^{2+} (blue line) successively. Inset: the fluorescence photograph of Au NCs in the absence (i) and presence (ii) of Ag^+ and AuAg NCs with Hg^{2+}. (iii) upon excitation under a UV lamp (365 nm). **b** Time course curves of Au NCs in the absence (black line) and presence of Ag^+ (red line) and the fluorescence quenching of AuAg NCs in the present of Hg^{2+} (blue line) in aqueous solution. **c** Photographs of Au NCs in aqueous buffer solutions taken under 365 nm UV illumination with various metal ions (15 mM) (up) and the subsequent addition of Ag^+ (2 mM) to the solution (below). **d** Emission response of Au NCs to various metal ions. **e** Photographs under UV light (365 nm) and **f** relative emission fluorescence (F/F_0) at 560 nm of aqueous AuAg NC solutions in the presence of 100 Mm of various metal ions [118] (published with permission from Zhang et al. (2015), ©2015 Elsevier B.V.). **g** Fluorescence titration of CASE-Au NCs versus Cu^{2+} ions and **h** application of the Stern Volmer relation for the CASE-Au NCs system using 100 μM $NaBH_4$, 12 μM Hg^{2+}, and 20 mM phosphate buffer at pH 7.4 solutions. **i** Fluorescence titration of CASE-Au NCs versus Hg^{2+} ions and **j** application of the Stern Volmer relation for the CASE-Au NCs system using 50 μM EDTA, 7 μM Cu^{2+}, and 20 Mm phosphate buffer at pH 7.4 solutions [117] (published with permission from Jiang et al. (2021), ©2021 Elsevier B.V.)

Quantitative detection of highly reactive oxygen species

Highly reactive oxygen species (hROS), such as hydroxyl (•OH), hypochlorite (ClO^-), and peroxynitrite $(ONOO)^-$) [127], exhibit strong oxidation characteristics that enable them to directly oxidize nucleic acids [78], proteins, and lipids, potentially causing severe damage within cells [128]. Excessive accumulation of hROS can lead to oxidative stress and has been associated with various pathological conditions, including cardiovascular disease [129], cancer, and nervous system diseases [130]. Therefore, the development of a probe for visualizing hROS is valuable for elucidating the biological functions and potential molecular mechanism of these hROS and could hold potential as a tool for medical diagnosis and research [131]. Au NCs can play a role in the detection of hROS. The fluorescence of the Au NCs can be sensitively and selectively quenched by these hROS. In addition, Au NCs can be utilized as nanoenzymes for specific catalytic roles.

Chen et al. employed Au NCs for the visualization and monitoring of hROS in living cells and designed a double-emission fluorescent nanocomposite (DEFN) as a

nanosensor for hROS living cell imaging [132]. Figure 6a illustrates the schematic diagram of the assembly of coronal nanoparticles into DEFN. Coronal nanoparticles are composed of a core-wrapped silica particle and multiple satellite Au NCs. For instance, Fig. 6b shows the fluorescence emission spectra of Au NCs (red) and DEFN (cyan). DEFN exhibits a typical double-emission spectrum with a wavelength difference of 130 nm, indicating that DEFN has a superior resolution for ratio detection and imaging analysis [133]. The fluorescence spectral response of DEFN to different concentrations of •OH is shown in Fig. 6c. With the increase of hROS concentration, the fluorescence intensity at 435 nm remains virtually unchanged, while the fluorescence intensity at 565 nm decreases, and the resolvable fluorescence color of DEFN shifts from red–purple to blue [134]. The relationship between the fluorescence intensity ratio at 435 and 565 nm and hROS concentration was analyzed, revealing a linear relationship, and the LODs for •OH, $ONOO^-$, and ClO^- were determined to be 0.03, 0.2, and 0.5 μM, respectively (Fig. 6d), which spans its physiological concentration range, demonstrating DEFN as an optimal ratio sensor for quantitative hROS [135]. Moreover, in the presence of other reactive oxygen species and common species in the biological matrix, further examination of fluorescence response revealed that these components had a minimal quenching effect on DEFN (Fig. 6e), thereby corroborating the high selectivity of DEFN for quantitative analysis of hROS.

Investigating the capacity of DEFN to visualize hROS in living cells facilitates its application in biological studies (Fig. 6f). Upon incubation of HeLa cells with DEFN, a conspicuous fluorescent signal with characteristic cytosolic co-localization was observed in both the blue and red channels (Fig. 6f (i)) [136]. Subsequently, the denitrified HeLa cells were treated with different reactive oxygen species to assess their reactivity (Fig. 6f (ii), (iii), (iv)). As illustrated in Fig. 6f (ii), following incubation of the cells loaded with DEFN with H_2O_2, strong fluorescence signals were observed on the blue and red channels, similar those to Fig. 6f (i), which proved that Au NCs maintained high fluorescence without oxidation [137]. In contrast, after incubation with HClO, the fluorescence signal almost disappeared in the

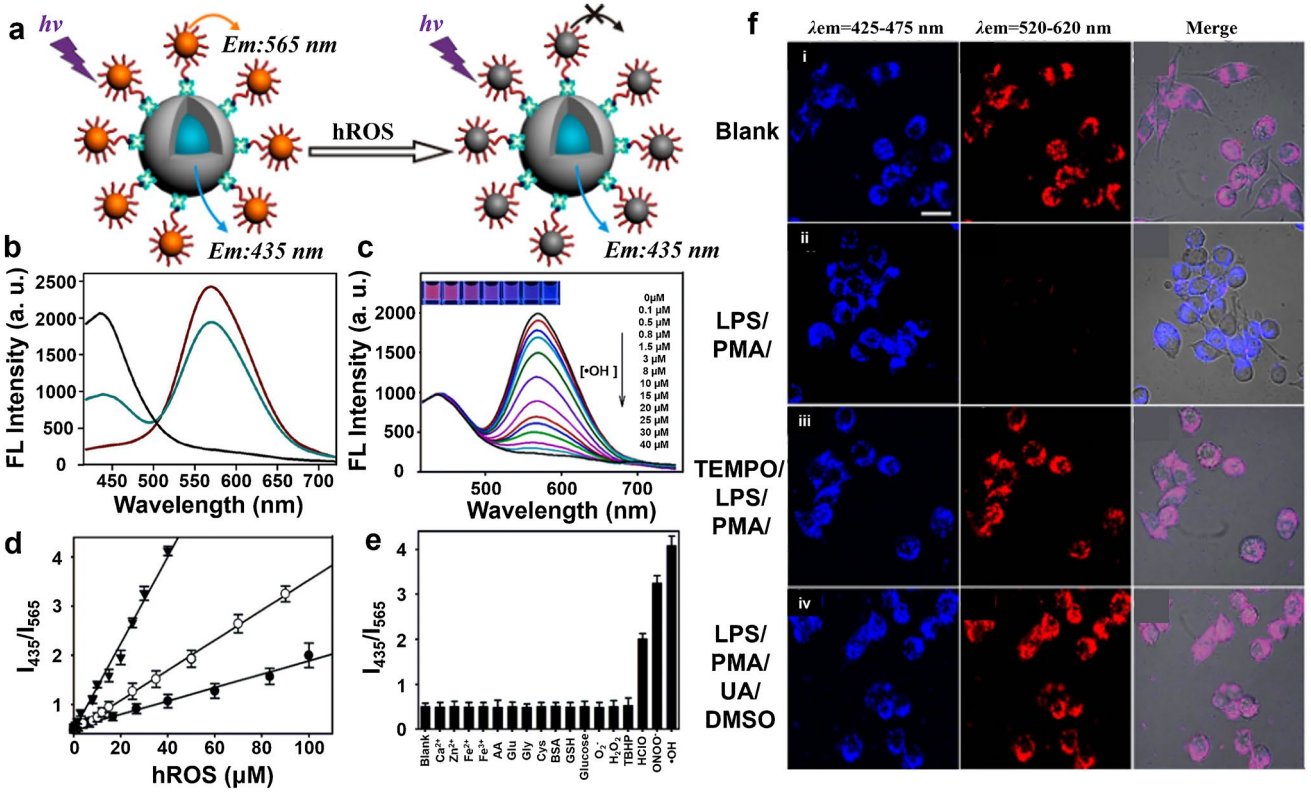

Fig. 6 Au NCs for the quantitative detection of highly reactive oxygen species (hROS). **a** hROS detection using the DEFN constructed. **b** Fluorescence emission spectra of dye-encapsulated silica nanoparticles (black), Au NCs (red), and DEFN (cyan). The excitation wavelength is 405 nm. **c** Fluorescence spectral responses of the DEFN to •OH of varying concentrations. The excitation wavelength was 405 nm. The inset is a photograph of fluorescence. **d** Working curves of the DEFN-based ratiometric sensor in response to hROS. •OH (triangle), $ONOO^-$ (circle), and ClO^- (dot). **e** Ratiometric responses of the DEFN sensor to hROS (100 μM ClO^-, 90 μM $ONOO^-$, and 40 μM •OH) and different coexistents (1 mM). **f** Confocal fluorescence microscopy images of RAW 264.7 cells. Scale bar, 20 μm [132] (published with permission from Chen et al. (2013), ©2013 American Chemical Society)

red channel, while a bright image was still visible in the blue channel (Fig. 6f (iii)), suggesting that HClO could quickly and substantially oxidize Au NCs and quench the fluorescence of Au NCs. The response of the DEFN sensor to $ONOO^-$ is similar to that of HClO (Fig. 6f (iv)) [138]. The results of live cell imaging showed that DEFN exhibited high selectivity and sensitivity for hROS.

Based on the above-mentioned properties, the DEFN sensor based on Au NCs demonstrates high sensitivity and selectivity for hROS. In addition, the fluorescence signal is strong and stable, providing the possibility for high-contrast imaging and possessing promising potential for fluorescence sensing and biological detection [139].

Quantitative detection of cysteine

Cysteine (Cys), a common amino acid in organisms, is a natural component of glutathione and contains active sulfhydryl (-SH) [140]. It can protect sulfhydryl protease and poisoned liver parenchymal cells, stimulate hematopoietic function [141], increase leukocytes, and promote the repair of skin damage. The quantitative detection of cysteine provides a convenient detection [142] method for the diagnosis of heart disease [79], sepsis [143], HIV, and other cysteine-related diseases.

Yu et al. designed a system utilizing carbon dots (CDs) and Au NCs@GSH as an idea donor and acceptor in the Förster resonance energy transfer (FRET) complex, serving as a ratio probe. This method has been successfully applied to the detection of cysteine [144]. As illustrated in Fig. 7a, the fluorescence spectrum monitoring diagram of the electrostatic binding process demonstrates that the emission intensity of CDs at 465 nm differs from Au NCs@GSH, which exhibits gradual quenching with increasing doping amount. At the same time, the fluorescence intensity of Au NCs@GSH at 605 nm increased significantly [145]. Therefore, the intensity ratio at both wavelengths increases significantly with the increase of the concentration of Au NCs (Fig. 7b), which can be explained well with the FRET model. The emission intensity at 465 nm of CD–Au NCs after adding different amounts of cysteine remains virtually unchanged, while the emission intensity at 605 nm gradually decreases or even nearly quenches (Fig. 7c) [146]. Furthermore, the fluorescence intensity ratio at 605–465 nm (I_{605}/I_{465}) demonstrates a nearly linear relationship with cysteine concentration when the addition amount of cysteine is less than 60 nm (Fig. 7d). This finding indicates that the FRET complex is an excellent ratio probe for the detection of cysteine [147]. The addition of various amino acids to the solution containing the CD–Au NCs complex revealed

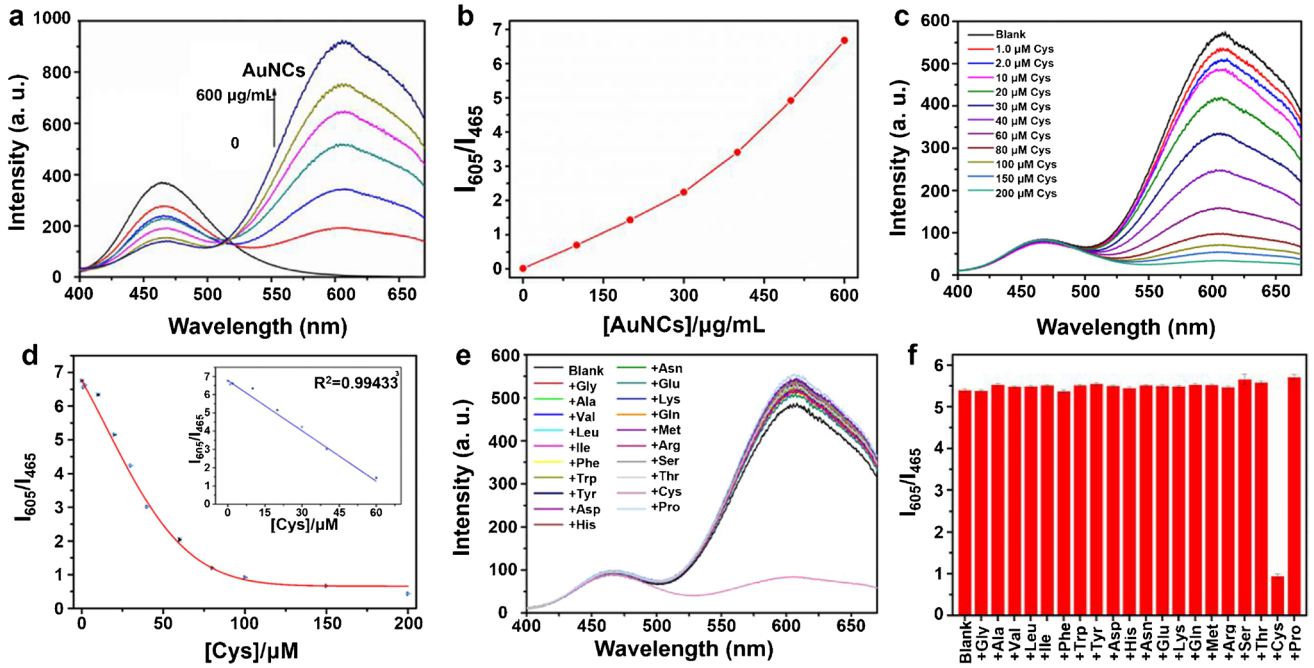

Fig. 7 CD–Au NCs@GSH for the quantitative detection of Cys. **a** The fluorescence spectra of 250 μg/mL CDs in water were titrated with different amounts of Au NCs@GSH (0–600 μg/mL). **b** The related ratio changes of fluorescence intensity at 605–465 nm (λ_{ex} = 345 nm). **c** Fluorescence spectra of CD–Au NCs (50 and 100 μg/mL) in HEPES-NaOH buffer solution (pH = 7.4) which were measured 60 min before and after adding different amounts of cysteine (Cys, from 1.0 to 200 μM). **d** The plot of the fluorescence intensity ratio changes with the concentration of cysteine (λ_{ex} = 345 nm). **e** The comparison of fluorescence spectra of CD–Au NCs (50 and 100 μg/mL) in the presence of different kinds of amino acids (100 μM) in HEPES-NaOH buffer solution (pH = 7.4). **f** The corresponding intensity ratio at 605 and 465 nm changes [144] (published with permission from Yu et al. (2018), ©2018 Elsevier B.V.)

no significant fluorescence reduction, except for cysteine (Fig. 7e, f). This finding confirms the excellent selectivity of CD–Au NCs for the detection of cysteine.

Based on the above property analysis, the FRET complex assembled by CD–Au NCs provides an efficient cysteine detection method with very simple sample preparation, ratio response, high selectivity, high sensitivity, and strong anti-interference, providing a method for accurate measurement of cysteine and a potential strategy for clinical detection [148].

Quantitative detection of enzymes

The enzyme, a type of biocatalyst, plays a crucial role in regulating various catalytic processes, including biological metabolism, nutrition, and energy conversion [149]. These properties of enzymes enable the complex material metabolism process in cells to proceed in an orderly manner, allowing material metabolism to adapt to normal physiological function [150]. Genetic defects or other factors that reduce enzyme activity may lead to abnormal reactions catalyzed by the enzyme [151], disorder material metabolism, and even disease [152]. For instance, excessive levels of xanthine can result in gout and uric acid deposition in the kidney in the form of stones [153], causing renal damage [142]. This is because xanthine is a precursor of uric acid, which is produced from xanthine by xanthine oxidase (XOD) enzymatic reaction [154]. Serum alkaline phosphatase (ALP) level is also closely associated with bone disease, diabetes, breast cancer, prostate cancer [155], and hepatitis [156]. Therefore, it is of great significance for the biological quantitative detection of enzymes.

Zhang et al. reported a comprehensive single-atom substitution method to create artificial enzymes based on mercaptopropionic acid (MPA)-protected Au NCs, namely, clusterzymes, which can achieve catalytic selectivity toward glutathione peroxidase, catalase, and superoxide dismutase nitrogen-related signaling molecules [157]. Wang et al. developed a xanthine colorimetric detection method based on BSA-stabilized Au NCs as a peroxidase simulant [157]. As with natural enzymatic-catalyzed reactions, there was a strong dependence between the initial reaction rate and hydrogen peroxide concentration. Figure 8a showed that the reaction catalyzed by BSA-Au nanoclusters was inhibited at high hydrogen peroxide concentrations (> 150 mM), while a linear relationship existed at lower hydrogen peroxide concentrations. The detection mechanism involves that Au BSA catalyzes TMB as a peroxidase simulant in the presence of H_2O_2, quickly forming a blue charge-transfer complex and causing the color change of the reaction system [158]. As shown in Fig. 8b, the absorbance of the system increases with the increase of H_2O_2 concentration. Under the optimum conditions (pH = 3.0 and 40 ℃), the calibration curve of absorbance at 652 nm and H_2O_2 concentration is linear from 5.0×10^{-7} to 2.0×10^{-5} M with the LOD of 2.0×10^{-8} M (Fig. 8b). Figure 8c demonstrates a linear response between the absorbance (652 nm) and xanthine concentration in the range of 1×10^{-6} to 2×10^{-4} M (R = 0.999) [159]. The above analysis indicates that the system exhibits high sensitivity and selectivity for xanthine and can be used to detect xanthine in buffer solution or urine and human serum samples.

Liu et al. developed an open fluorescent sensor to simply and sensitively detect the activity of alkaline phosphatase (ALP) through the internal filtration effect (IFE) of p-nitrophenyl phosphate (PNPP) on the fluorescence of Au NCs [160]. The sensor's detection mechanism is based on the competitive absorption of PNPP, which reduces the fluorescence measurement value of Au NCs. In the presence of ALP, PNPP is catalytically hydrolyzed to nitrophenol (PNP), thereby reducing competitive absorption and restoring the reduced emission of Au NCs, enabling ALP detection [161]. Figure 8d displays the fluorescence emission spectrum of Au NCs under the condition of increasing ALP concentration. It can be observed that the fluorescence of Au NCs gradually recovers with the increase of ALP concentration from 0 to 300 U/L, which is the result of PNPP hydrolysis by ALP. Figure 8e represents the relationship between $F\text{-}F_0$ and ALP concentration between 0 and 300 U/L, showing a linear fitting equation of $F\text{-}F_0 = 26.14\,[ALP] + 12.14$, U/L with a corresponding linear correlation coefficient of 0.98. The LOD of ALP is as low as 0.002 U/L (S/N = 3), proving the sensor's high detection sensitivity for ALP [162]. The sensor was further tested for the detection of galactosidase, glucose oxidase, thrombin, pepsin, trypsin, and other metal ions (Mg^{2+}, Zn^{2+}, Fe^{3+}, K^+, Na^+, Ca^{2+}, 100 μM). The addition of 10 U/L ALP to these solutions resulted in significant fluorescence recovery (Fig. 8f), indicating the high selectivity of this sensing method for ALP. Na_3VO_4, a common ALP inhibitor, is added to the ALP reaction system, limiting the fluorescence recovery level in proportion to the amount of inhibitor (Fig. 8g, h) [163]. The LOD of Na_3VO_4 (S/N = 3) is 0.06 μM (Fig. 8h). These results indicate that the developed sensing approach could be employed for the screening of ALP inhibitors in drug discovery. The fabricated fluorescent sensor is employed for the quantification of human serum samples ALP activity, assessing the reliability of the established method in serum samples. As shown in Fig. 8i, the results obtained by this sensing method exhibit a high degree of concurrence with those obtained from clinical methods [164]. These results show that the open fluorescent sensor has high sensitivity and selectivity for ALP determination of actual samples, which provides a new way for ALP sensing in clinical diagnosis [165].

Based on the above analysis, Au NCs exhibit considerable sensitivity and selectivity for the quantitative detection of some enzymes and can be effectively utilized in their biological detection, which provides the possibility for the

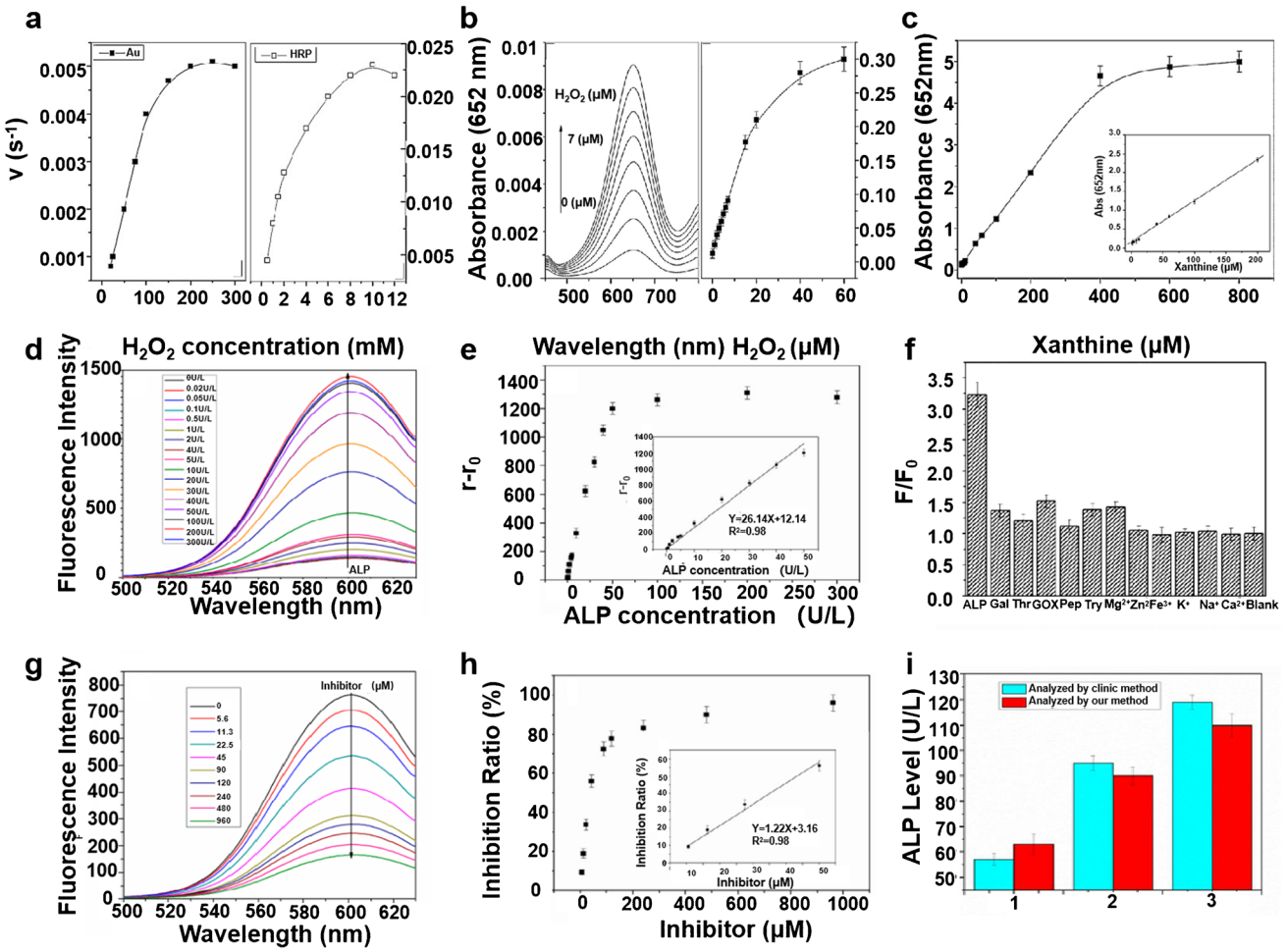

Fig. 8 Au NCs for the quantitative detection of enzymes. **a** The typical absorption spectrum of the TMB solution in the presence of H_2O_2 at various concentrations using BSA-Au NCs as an artificial enzyme. **b** Linear calibration plot between the absorbance at 652 nm and concentration of H_2O_2. Inset: linear calibration plot for H_2O_2. **c** A dose–response curve for xanthine detection using XOD and BSA-Au NCs. Inset: linear calibration plot for xanthine in the range 1×10^{-6} to 2×10^{-4} M [157] (published with permission from Wang et al. (2011), ©2011 Elsevier B.V.). **d** Fluorescence emission spectra of Au NCs and **e** plots of F–F_0 versus ALP concentration from 0 to 300 U/L (inset: its corresponding linear relationship from 0.02 to 50 U/L). **f** Selectivity of ALP assays in the presence of different enzymes and different metal ions. **g** Fluorescence intensity of Au NCs in the presence of various concentrations of Na_3VO_4 and their calibration plots. **h** The inhibitors were incubated with 20 U/L enzymes, 1 mM PNPP, and 0.1 μM $MgSO_4$. **i** Detection of ALP in three adult volunteers serums by the clinic method and our method [160] (published with permission from Liu et al. (2016), ©2016 American Chemical Society)

clinical detection of enzyme-related diseases and expands the potential application of metal nanoclusters.

Quantitative detection of human immunodeficiency virus (HIV)

Acquired immune deficiency syndrome (AIDS) is a devastating infectious disease, resulting from infection by the AIDS virus (HIV). HIV is a virus that attacks the human immune system, primarily assaulting $CD4^+$ T lymphocytes, which are crucial to immune function. This destruction of cells in large quantities leads to a significant loss of immune function [166]. Therefore, the human body is predisposed to various diseases and malignant tumors with high mortality. The average incubation period of HIV in the human body is 8–9 years. During the incubation period of the AIDS virus, individuals can live and work without any symptoms for many years [167]. However, once the virus progresses to AIDS, patients will have various clinical manifestations in a short time. Currently, there is no effective treatment or drug available for AIDS. Therefore, the early detection of HIV is vital for inhibiting the progression of the disease.

Kurdekar et al. employed streptavidin-bound Au NCs (Au NC–SA) for Au NC immunoassay (GNCIA) to detect HIV-1 p^{24} antigen to identify early HIV infection cases [168]. The immunoassay of Au NCs employed a sandwich

immunoassay format, consisting of an antibody–antigen–antibody sandwich complex, to detect the chemical reaction between antibody and Au NC–SA based on a biotinylation detector, as schematically depicted in Fig. 9a. As illustrated in Fig. 9b, the UV-Vis and PL of glutathione functionalized Au NCs presented that the Au NCs exhibit high fluorescence intensity with a strong emission peak at 615 nm [169]. The primary interaction involved in the detection process is the strong noncovalent chemical interaction between biotin and streptavidin, which fixes the fluorophore on the sandwich complex. The emitted fluorophore signal intensity is directly proportional to the quantity of Au NC–SA under excitation. The quantity of Au NC–SA is directly proportional to the presence of HIV-1 p^{24} antigen in the sample, thus determining the signal intensity [170]. Subsequently, the fluorescence signal intensity was recorded using a spectrophotometer, and a calibration curve between the signal intensity and the concentration of purified HIV-1 p^{24} antigen was constructed using the measured data. As shown in Fig. 9c, an excellent linear correlation between the concentration of HIV-1 p^{24} and the fluorescence intensity in GNCIA is evident, which is further confirmed by the value $R^2 = 0.99941$ [171]. The study assessed the sensitivity of GNCIA by testing the samples from infected individuals (HIV-positive samples). For instance, Fig. 9d displays the GNCIA results for 10 randomly selected HIV-positive samples, demonstrating a large LOD and thereby proving the high sensitivity of GNCIA. Figure 9e presents the results of GNCIA results of HIV-negative samples, minimum positive test samples, and blank control. Figure 9f employs 10 HBV-positive/HIV-negative and 10 HCV-positive/HIV-negative plasma samples to contrast the intensity with the minimum positive test samples and blank samples, demonstrating that GNCIA exhibits excellent selectivity for the identification of samples other than HIV-positive samples [166, 170], which validates that the detection method is specific for p^{24} antigen and is minimally influenced by the cross-reactivity with other virus particles and biomolecules.

Unlike previously reported detection methods, GNCIA can achieve high sensitivity without complex equipment and expensive reagents [172]. Characterized by stable signal intensity and a high signal-to-noise ratio, GNCIA represents a highly sensitive immunoassay method. GNCIA has the potential to develop into a rapid and ultra-sensitive test platform for clinical diagnosis and laboratory research in a resource-limited environment.

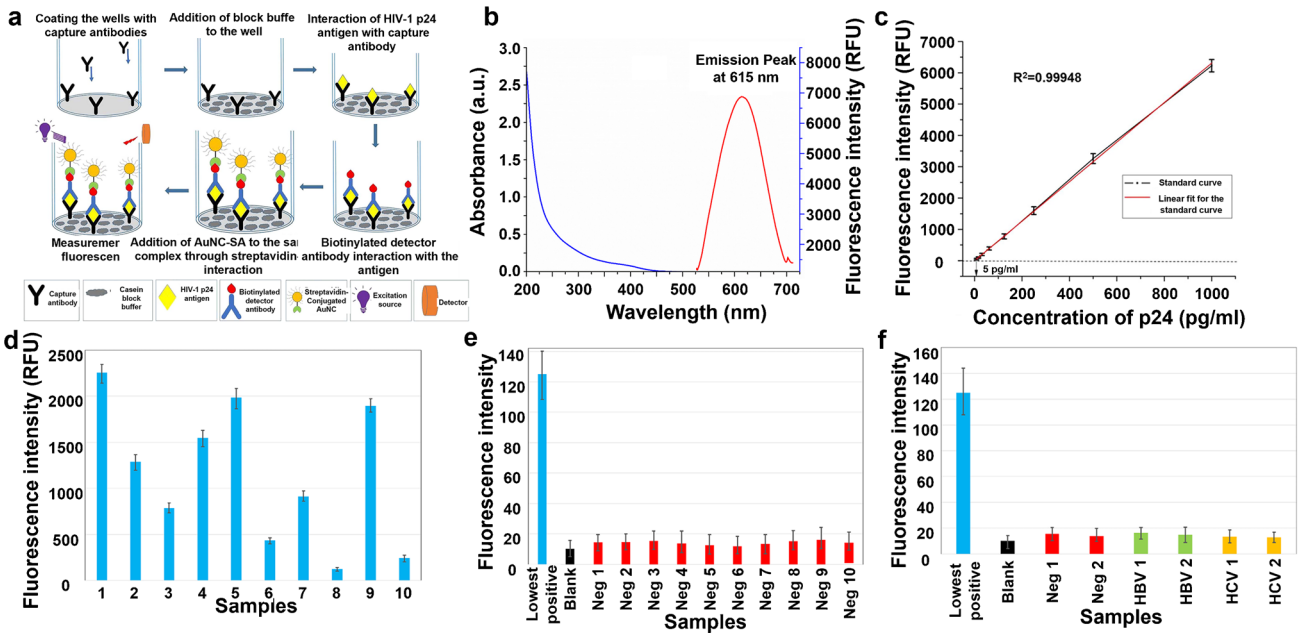

Fig. 9 Au NCs for the quantitative detection of HIV. **a** Schematic representation of GNCIA in the detection of HIV-1 p24 antigen. **b** Absorption and emission spectra of Au NCs. **c** Calibration plot of GNCIA. **d** Results of GNCIA for the 10 samples tested as HIV positive were chosen at random (blue bars). **e** Results of GNCIA for two randomly chosen samples tested as HIV negative in comparison with the lowest positive tested sample and blank. Blue and black bars indicate the intensity of the HIV-positive sample and the blank. **f** Results of GNCIA for two randomly chosen HIV-negative, HBV-positive/HIV-negative, and HCV-positive/HIV-negative samples, respectively, in comparison with the intensity of the lowest positive tested sample and blank. Blue and black bars indicate the intensity of the HIV-positive sample and the blank, while the red, green, and yellow bars indicate HIV-negative, HBV-positive/HIV-negative, and HCV-positive/HIV-negative samples, respectively [168] (published with permission from Kurdekar et al. (2023), ©2023 American Association for the Advancement of Science)

Conclusions

Au NCs possess several advantages. The simple one-pot synthesis method enables the easy fabrication of Au NCs [4]. With an impressive quantum yield of up to 100% and enhanced luminescence efficiency, Au NCs exhibit a more efficient luminescence process [173]. The gold nanoclusters with a size smaller than the renal clearance threshold of 5.5 nm can be rapidly excreted through the urinary system without cumulative toxicity, providing ideal biosafety [174]. Complex excited state processes and small absorption coefficients for band-edge leaps lead to large Stokes shifts and long PL lifetimes widely observed in gold nanoclusters [1, 175]. Therefore, research on their synthesis [176], characterization, bioconjugation [177], and applications of Au NCs is a thriving and evolving field [23]. Fluorescence Au NCs can be utilized for the quantitative detection of inorganic and metal ions, effectively monitoring the ion content [178], which helps prevent and detect the possibility of related diseases [179]. They can be employed for the quantitative detection of common biological macromolecules such as amino acids and enzymes and play a good monitoring role in controlling biological material metabolism and normal physiological function [7]. Additionally, Au NCs can be directly employed for pathogen detection of some disease-related viruses and intercepted during the early stage of the disease [180]. Meanwhile, gold nanoclusters can also be utilized for preoperative tumor localization, intraoperative surgical guidance, and postoperative prognostic assessment, showing promise for imaging and therapy [39]. Therefore, Au NCs exhibit great potential for clinical applications.

Significant advancements have been made in Au NC structure and fluorescence tune as well as biological detection methods [181] and show potential for biomedicine. However, there are several areas to improve, such as the short emission wavelength and low brightness of the developed Au NCs [182]. At present, the commonly utilized Au NCs for biological detection are primarily in the NIR-I window in 700–900 nm with limited resolution [183] and have low imaging performance [3]. While the NIR-II region exhibits exceptional spatial–temporal resolution and high tissue penetration with a maximum penetration depth of 1 ~ 2 mm [184]. It is well documented that the physiochemical properties of Au NCs are largely dependent on the composition, surface, and structure [3, 15]; thus, there are several ways for the improvement. First, NIR-II Au NCs with long emission wavelengths can be designed by altering the ligands and doping metal elements combined to achieve high imaging resolution and deep penetration [15, 19]. Second, single-atom doping can introduce a new catalytic center to boost the enzymatic activities of Au NCs and improve the potential as nanozymes for detection and treatment usage in biomedicine. Finally, biosafety is a key factor in clinical use [32, 39]; the biocompatibility of Au NCs can be improved by optimizing ligands and constructing reasonable spatial structure [185]. It can be seen that Au NCs possess wide application prospects and great significance in the field of fluorescence sensing and biological detection [186]. The development of biosafety Au NCs with specific functions and applications in the medical field can promote clinical translation.

Author contribution Conceptualization, Xiao Dong Zhang and Kexin Tan; investigation, Kexin Tan and Xiaoyu Mu; writing, original draft, Kexin Tan and Huizhen Ma; writing, review and editing, Kexin Tan and Huizhen Ma; formal analysis, Zhidong Wang; validation, Qi Wang and Hao Wang; supervision, Xiao Dong Zhang and Hao Wang.

Funding This work was financially supported by the National Key Research and Development Program of China (2021YFF1200700), the National Natural Science Foundation of China (Grant Nos. 91859101, 81971744, U1932107, 82001952, 11804248, 82302361, and 82302381), the Outstanding Youth Funds of Tianjin (2021FJ-0009), the National Natural Science Foundation of Tianjin (Nos. 19JCZDJC34000, 20JCYBJC00940, 21JCYBJC00550, 21JCZDJC00620, and 21JCYBJC00490), the Innovation Foundation of Tianjin University, and CAS Interdisciplinary Innovation Team (JCTD-2020-08).

Declarations

Competing interests The authors declare no competing interests.

References

1. Liu H, Li Y, Sun S, Xin Q, Liu S, Mu X, et al. Catalytically potent and selective clusterzymes for modulation of neuroinflammation through single-atom substitutions. Nat Commun. 2021;12(1):114.
2. Mu X, Wang J, He H, Li Q, Yang B, Wang J, et al. An oligomeric semiconducting nanozyme with ultrafast electron transfers alleviates acute brain injury. Sci Adv. 2021;7(46): eabk1210.
3. Sun S, Liu H, Xin Q, Chen K, Ma H, Liu S, et al. Atomic engineering of clusterzyme for relieving acute neuroinflammation through lattice expansion. Nano Lett. 2021;21(6):2562–71.
4. Chen K, Sun S, Wang J, Zhang X-D. Catalytic nanozymes for central nervous system disease. Coord Chem Rev. 2021;432: 213751.
5. Zhang Y, Ni S, Chong C, Xu J, Mu X, Zhang X-D. Biocatalysts at atom level: from coordination structure to medical applications. Appl Mater Today. 2021;23: 101029.
6. Zhou X, Huang S, Zhang D, Liu W, Gao W, Xue Y, et al. Gold nanocluster-based fluorescent microneedle platform toward visual detection of ATP. Anal Chem. 2023;95(32):12104–12.
7. Mu X, He H, Wang J, Long W, Li Q, Liu H, et al. Carbogenic nanozyme with ultrahigh reactive nitrogen species selectivity for traumatic brain injury. Nano Lett. 2019;19(7):4527–34.
8. Welsher K, Liu Z, Sherlock S, Robinson J, Chen Z, Daranciang D, et al. A route to brightly fluorescent carbon nanotubes for near-infrared imaging in mice. Nat Nanotechnol. 2009;4(11):773–80.

9. Li C, Li F, Zhang Y, Zhang W, Zhang X, Wang Q. Real-time monitoring surface chemistry-dependent behaviors of protein nanocages via encapsulating an NIR-II Ag_2S quantum dot. ACS Nano. 2015;9(12):12255–63.
10. Shao W, Chen G, Kuzmin A, Kutscher H, Pliss A, Ohulchanskyy T, et al. Tunable narrow band emissions from dye-sensitized core/shell/shell nanocrystals in the second near-infrared biological window. J Am Chem Soc. 2016;138(50):16192–5.
11. Hong G, Zou Y, Antaris A, Diao S, Wu D, Cheng K, et al. Ultrafast fluorescence imaging with conjugated polymer fluorophores in the second near-infrared window. Nat Commun. 2014;5:5206.
12. Wang S, Fan Y, Li D, Sun C, Lei Z, Lu L, et al. Anti-quenching NIR-II molecular fluorophores for in vivo high-contrast imaging and pH sensing. Nat Commun. 2019;10:1058.
13. Liu S, Li Y, Kwok R, Lam J, Tang B. Structural and process controls of AIEgens for NIR-II theranostics. Chem Sci. 2021;12(10):3427–36.
14. Li B, Zhao M, Zhang F. Rational design of near-infrared-II organic molecular dyes for bioimaging and biosensing. ACS Mater Lett. 2020;2(8):905–17.
15. Ma H, Zhang X, Liu L, Huang Y, Sun S, Chen K, et al. Bioactive NIR-II gold clusters for three-dimensional imaging and acute inflammation inhibition. Sci Adv. 2023;9(31):eadh7828.
16. Liu P, Mu X, Zhang X-D, Ming D. The near-infrared-II fluorophores and advanced microscopy technologies development and application in bioimaging. Bioconjug Chem. 2019;31(2):260–75.
17. Chen L, Wang C, Yuan Z, Chang H. Fluorescent gold nanoclusters: recent advances in sensing and imaging. Anal Chem. 2015;87(1):216–29.
18. Liu H, Hong G, Luo Z, Chen J, Chang J, Gong M, et al. Atomic-precision gold clusters for NIR-II imaging. Adv Mater. 2019;31(46):1901015.
19. Huang Y, Chen K, Liu L, Ma H, Zhang X, Tan K, et al. Single atom-engineered NIR-II gold clusters with ultrahigh brightness and stability for acute kidney injury. Small. 2023;19(30):2300145.
20. Bian P, Zhang J, Wang J, Yang J, Wang J, Liu H, et al. Enhanced catalysis of ultrasmall Au-MoS 2 clusters against reactive oxygen species for radiation protection. Sci Bull. 2018;63(14):925–34.
21. Qian H, Jiang DE, Li G, Gayathri C, Das A, Gil RR, et al. Monoplatinum doping of gold nanoclusters and catalytic application. J Am Chem Soc. 2012;134(39):16159–62.
22. Chib R, Butler S, Raut S, Shah S, Borejdo J, Gryczynski Z, et al. Effect of quencher, denaturants, temperature and pH on the fluorescent properties of BSA protected gold nanoclusters. J Lumin. 2015;168:62–8.
23. Liu S, Zhao Y, Hao W, Zhang X-D, Ming D. Micro- and nanotechnology for neural electrode-tissue interfaces. Biosens Bioelectron. 2020;170: 112645.
24. Zheng K, Setyawati MI, Leong DT, Xie J. Antimicrobial gold nanoclusters. ACS Nano. 2017;11(7):6904–10.
25. Zheng Y, Wu J, Jiang H, Wang X. Gold nanoclusters for theranostic applications. Coord Chem Rev. 2021;431: 213689.
26. Loynachan CN, Soleimany AP, Dudani JS, Lin Y, Najer A, Bekdemir A, et al. Renal clearable catalytic gold nanoclusters for in vivo disease monitoring. Nat Nanotechnol. 2019;14(9):883–90.
27. Yao Q, Yuan X, Fung V, Yu Y, Leong DT, Jiang De, et al. Understanding seed-mediated growth of gold nanoclusters at molecular level. Nat Commun. 2017;8(1):927.
28. Jin R. Quantum sized, thiolate-protected gold nanoclusters. Nanoscale. 2010;2(3):343–62.
29. Yougbare S, Chang T, Tan S, Kuo J, Hsu P, Su C, et al. Antimicrobial gold nanoclusters: recent developments and future perspectives. Int J Mol Sci. 2019;20(12):2924.
30. Chen J, Liu L, Liu H, Li Y, Wang J, Mu X, et al. Ultrabright bimetallic AuAg complex: from luminescence mechanism to biological application. J Innov Opt Health Sci. 2020;13(05):2041001.
31. Zhang K, Song H, Su Y, Li Q, Sun M, Lv Y. Flower-like gold nanoparticles for in situ tailoring luminescent molecules for synergistic enhanced chemiluminescence. Anal Chem. 2022;94(25):8947–57.
32. Wang J, Mu X, Li Y, Xu F, Long W, Yang J, et al. Hollow PtPdRh nanocubes with enhanced catalytic activities for in vivo clearance of radiation-induced ROS via surface-mediated bond breaking. Small. 2018;14(13):1703736.
33. Zheng Y, Lai L, Liu W, Jiang H, Wang X. Recent advances in biomedical applications of fluorescent gold nanoclusters. Adv Colloid Interface Sci. 2017;242:1–16.
34. Qu X, Li Y, Li L, Wang Y, Liang J, Liang J. Fluorescent gold nanoclusters: synthesis and recent biological application. J Nanomaterials. 2015;784097:23.
35. Kong X, Tian J, Fang Y, Chen T, Yu R, He J-Y, et al. Terbium metal-organic framework/bovine serum albumin capped gold nanoclusters-based dual-emission reverse change ratio fluorescence nanoplatform for fluorimetric and colorimetric sensing of heparin and chondroitin sulfate. Sens Actuators B Chem. 2022;356: 131331.
36. Chen L, Liu D, Peng J, Du Q, He H. Ratiometric fluorescence sensing of metal-organic frameworks: tactics and perspectives. Coord Chem Rev. 2020;404: 213113.
37. Zhao R, Liu H, Li Y, Guo M, Zhang X-D. Catalytic nanozyme for radiation protection. Bioconjug Chem. 2021;32(3):411–29.
38. Liu J, Sun YQ, Huo Y, Zhang H, Wang L, Zhang P, et al. Simultaneous fluorescence sensing of Cys and GSH from different emission channels. J Am Chem Soc. 2014;136(2):574–7.
39. Wang H, Mu X, Yang J, Liang Y, Zhang X-D, Ming D. Brain imaging with near-infrared fluorophores. Coord Chem Rev. 2019;380:550–71.
40. Tang Z, Chen F, Wang D, Xiong D, Yan S, Liu S, et al. Fabrication of avidin-stabilized gold nanoclusters with dual emissions and their application in biosensing. J Nanobiotechnology. 2022;20(1):306.
41. Qian S, Wang Z, Zuo Z, Wang X, Wang Q, Yuan X. Engineering luminescent metal nanoclusters for sensing applications. Coord Chem Rev. 2022;451: 214268.
42. Zhou X, Wang X, Shang L. Ratiometric fluorescence and visual sensing of ATP based on gold nanocluster-encapsulated metal-organic framework with a smartphone. Chin Chem Lett. 2023;34(8): 108093.
43. Wu Y, Jin X, Ashrafzadeh Afshar E, Taher MA, Xia C, Joo S-W, et al. Simple turn-off fluorescence sensor for determination of raloxifene using gold nanoparticles stabilized by chitosan hydrogel. Chemosphere. 2022;305: 135392.
44. Zhou S, Xu H, Gan W, Yuan Q. Graphene quantum dots: recent progress in preparation and fluorescence sensing applications. RSC Adv. 2016;6(112):110775–88.
45. Dornsiepen E, Eussner JP, Rosemann NW, Chatterjee S, Dehnen S. Syntheses and properties of gold-organotin sulfide clusters. Inorg Chem. 2017;56(18):11326–35.
46. Mohanty JS, Chaudhari K, Sudhakar C, Pradeep T. Metal-ion-induced luminescence enhancement in protein protected gold clusters. J Phys Chem C. 2019;123(47):28969–76.
47. Croissant JG, Zhang D, Alsaiari S, Lu J, Deng L, Tamanoi F, et al. Protein-gold clusters-capped mesoporous silica nanoparticles for high drug loading, autonomous gemcitabine/doxorubicin co-delivery, and in-vivo tumor imaging. J Control Release. 2016;229:183–91.
48. Wu Z, Yao Q, Zang S, Xie J. Directed self-assembly of ultrasmall metal nanoclusters. ACS Mater Lett. 2019;1(2):237–48.
49. Chevrier DM, Thanthirige VD, Luo Z, Driscoll S, Cho P, MacDonald MA, et al. Structure and formation of highly

luminescent protein-stabilized gold clusters. Chem Sci. 2018;9(10):2782–90.
50. Sargazi S, Fatima I, Hassan Kiani M, Mohammadzadeh V, Arshad R, Bilal M, et al. Fluorescent-based nanosensors for selective detection of a wide range of biological macromolecules: a comprehensive review. Int J Biol Macromol. 2022;206:115–47.
51. Yamazoe S, Takano S, Kurashige W, Yokoyama T, Nitta K, Negishi Y, et al. Hierarchy of bond stiffnesses within icosahedral-based gold clusters protected by thiolates. Nat Commun. 2016;7:10414.
52. Dou X, Yuan X, Yu Y, Luo Z, Yao Q, Leong D, et al. Lighting up thiolated Au@Ag nanoclusters aggregation-induced emission. Nanoscale. 2014;6(1):157–61.
53. Pyo K, Thanthirige V, Kwak K, Pandurangan P, Ramakrishna G, Lee D. Ultrabright luminescence from gold nanoclusters: rigidifying the Au(I)-thiolate shell. J Am Chem Soc. 2015;137(25):8244–50.
54. Li H, Zhu W, Wan A, Liu L. The mechanism and application of the protein-stabilized gold nanocluster sensing system. Analyst. 2017;142(4):567–81.
55. Wu Z, Yao Q, Chai O, Ding N, Xu W, Zang S, et al. Unraveling the impact of gold(i)-thiolate motifs on the aggregation-induced emission of gold nanoclusters. Angew Chem Int Ed. 2020;59(25):9934–9.
56. Ai P, Mauro M, Danopoulos AA, Muñoz-Castro A, Braunstein P. Dual emission of a cyclic hexanuclear gold(i) complex. interplay between Au_3 and Au_2 ligand-supported luminophores. The Journal of Physical Chemistry C. 2018;123(1):915–21.
57. Mo L, Jia J, Sun L, Wang Q. Solvent-induced intercluster rearrangements and the reversible luminescence responses in sulfide bridged gold(i)–silver(i) clusters. Chem Commun. 2012;48(69):8691.
58. Yao L, Yam V. Dual emissive gold(I)-sulfido cluster framework capable of benzene-cyclohexane separation in the solid state accompanied by luminescence color changes. J Am Chem Soc. 2021;143(6):2558–66.
59. Liu C, Wei X, Chen Y, Wang H, Ge J, Xu Y, et al. Tetradecanuclear and octadecanuclear gold(i) sulfido clusters: synthesis, structures, and luminescent selective tracking of lysosomes in living cells. Inorg Chem. 2019;58(6):3690–7.
60. Sheng X, Li E, Zhou Y, Zhao R, Zhu W, Huang F. Separation of 2-chloropyridine/3-chloropyridine by nonporous adaptive crystals of pillararenes with different substituents and cavity sizes. J Am Chem Soc. 2020;142(13):6360–4.
61. Xu G, Wu L, Chang X, Ang T, Wong W, Huang J, et al. Solvent-induced cluster-to-cluster transformation of homoleptic gold(I) thiolates between catenane and ring-in-ring structures. Angew Chem Int Ed. 2019;58(45):16297–306.
62. Yao L, Chen Z, Zhang K, Yam V. Heterochiral self-discrimination-driven supramolecular self-assembly of decanuclear gold(i)-sulfido complexes into 2D nanostructures with chiral anions-tuned morphologies. Angew Chem Int Ed. 2020;59(47):21163–9.
63. Agrawal S, Mysko RA, Nigra MM, Mohanty SK, Hoepfner MP. Plasmonic photocatalytic enhancement of l-cysteine self-assembled gold nanoparticle clusters for fenton reaction catalysis. Langmuir. 2021;37(11):3281–7.
64. Ebina A, Hossain S, Horihata H, Ozaki S, Kato S, Kawawaki T, et al. One-, two-, and three-dimensional self-assembly of atomically precise metal nanoclusters. Nanomaterials. 2020;10(6):1105.
65. Shi L, Zhu L, Guo J, Zhang L, Shi Y, Zhang Y, et al. Self-assembly of chiral gold clusters into crystalline nanocubes of exceptional optical activity. Angew Chem Int Ed. 2017;56(48):15397–401.
66. Wu Z, Du Y, Liu J, Yao Q, Chen T, Cao Y, et al. Aurophilic interactions in the self-assembly of gold nanoclusters into nanoribbons with enhanced luminescence. Angew Chem Int Ed. 2019;58(24):8139–44.
67. Huang R, Wei Y, Dong X, Wu X, Du C, Zang S, et al. Hypersensitive dual-function luminescence switching of a silver-chalcogenolate cluster-based metal-organic framework. Nat Chem. 2017;9(7):689–97.
68. Azubel M, Koivisto J, Malola S, Bushnell D, Hura G, Koh A, et al. Electron microscopy of gold nanoparticles at atomic resolution. Science. 2014;345(6199):909–12.
69. Chang H, Karan NS, Shin K, Bootharaju MS, Nah S, Chae SI, et al. Highly fluorescent gold cluster assembly. J Am Chem Soc. 2021;143(1):326–34.
70. Zhou M, Higaki T, Hu G, Sfeir M, Chen Y, Jiang D, et al. Three-orders-of-magnitude variation of carrier lifetimes with crystal phase of gold nanoclusters. Science. 2019;364:279–84.
71. Sakthivel N, Dass A. Aromatic thiolate-protected series of gold nanomolecules and a contrary structural trend in size evolution. Acc Chem Res. 2018;51(8):1774–83.
72. Xie Z, Sun P, Wang Z, Li H, Yu L, Sun D, et al. Metal-organic gels from silver nanoclusters with aggregation-induced emission and fluorescence-to-phosphorescence switching. Angew Chem Int Ed. 2020;59(25):9922–7.
73. Wang Z, Li Q, Tan L, Liu C, Shang L. Metal-organic frameworks-mediated assembly of gold nanoclusters for sensing applications. J Anal Test. 2022;6(2):163–77.
74. Gao Y, Wang C, Zhang C, Li H, Wu Y. Glutathione protected bimetallic gold-platinum nanoclusters with near-infrared emission for ratiometric determination of silver ions. Microchim Acta. 2021;188(2):50.
75. Huang J, Mo X, Fu H, Sun Y, Gao Q, Chen X, et al. Tyndall-effect-enhanced supersensitive naked-eye determination of mercury (II) ions with silver nanoparticles. Sens Actuators B Chem. 2021;344: 130218.
76. Araki J, Hida Y. Comparison of methods for quantitative determination of silver content in cellulose nanowhisker/silver nanoparticle hybrids. Cellulose. 2018;25(2):1065–76.
77. Du C, Liu B, Hu J, Li H. Determination of iodine number of activated carbon by the method of ultraviolet–visible spectroscopy. Mater Res Lett. 2021;285: 129137.
78. González J, Wang JA, Chen LF, Manríquez M, Salmones J, Limas R, et al. Quantitative determination of oxygen defects, surface Lewis acidity, and catalytic properties of mesoporous MoO_3/SBA-15 catalysts. J Solid State Chem. 2018;263:100–14.
79. Ruan SL, Zhou Y, Zhang M, Zhang HY, Wang YR, Hu P. Rapid determination of cysteine and chiral discrimination of D-/L-cysteine via the aggregation-induced emission enhancement of gold nanoclusters by Ag^+. Anal Chem. 2022;38(3):541–51.
80. Wu Z, Lu J, Fu Q, Sheng L, Liu B, Wang C, et al. A smartphone-based enzyme-linked immunochromatographic sensor for rapid quantitative detection of carcinoembryonic antigen. Sens Actuators B Chem. 2021;329: 129163.
81. An X, Tan Q, Pan S, Zhen S, Hu Y, Hu X. Determination of xanthine using a ratiometric fluorescence probe based on boron-doped carbon quantum dots and gold nanoclusters. Mikrochim Acta. 2022;189(4):148.
82. Zhou C, Wang N, Lv Y, Sun H, Wang G, Su X. Cascade reaction biosensor based on gold nanocluster decorated iron-cobalt oxide nanosheets as a superior peroxidase mimic for dual-mode detection of α-glucosidase and its inhibitor. Talanta. 2023;254: 124148.
83. Li Z, Liu R, Xing G, Wang T, Liu S. A novel fluorometric and colorimetric sensor for iodide determination using DNA-templated gold/silver nanoclusters. Biosens Bioelectron. 2017;96:44–8.
84. Islam S. Cyanide at the origin of metabolism. Nat Chem. 2022;14(2):123–5.

85. Razanamahandry L, Onwordi C, Saban W, Bashir A, Mekuto L, Malenga E, et al. Performance of various cyanide degrading bacteria on the biodegradation of free cyanide in water. J Hazard. 2019;380:19–20.
86. Bostelaar T, Vitvitsky V, Kumutirna J, Lewis B, Yadav P, Brunold T, et al. Hydrogen sulfide oxidation by myoglobin. J Am Chem Soc. 2016;138(27):8476–88.
87. Li S, Ma Q, Wang C, Yang K, Hong Z, Chen Q, et al. Near-infrared II gold nanocluster assemblies with improved luminescence and biofate for in vivo ratiometric imaging of H_2S. Anal Chem. 2022;94(5):2641–7.
88. Sokolov A, Nekrasov P, Shaposhnikov M, Moskalev A. Hydrogen sulfide in longevity and pathologies: inconsistency is malodorous. Ageing Res Rev. 2021;67: 101262.
89. Yu F, Huang H, Shi J, Liang A, Jiang Z. A new gold nanoflower sol SERS method for trace iodine ion based on catalytic amplification. Spectrochim Acta A Mol Biomol Spectrosc. 2021;255: 119738.
90. Jiang R, Zhang Y, Zhang Q, Li L, Yang L. Carbon dot/gold nanocluster-based fluorescent colorimetric paper strips for quantitative detection of iodide ions in urine. Acs Appl Nano Mater. 2021;4(9):9760–7.
91. Khan I, Niazi S, Yu Y, Mohsin A, Mushtaq B, Iqbal M, et al. Aptamer induced multicolored AuNCs-WS_2 "Turn on" FRET nano platform for dual-color simultaneous detection of aflatoxinb and zearalenone. Anal Chem. 2019;91(21):14085–92.
92. Chen Q, Yao Y, Liao J, Li J, Xu J, Wang T, et al. Subnanometer ion channel anion exchange membranes having a rigid benzimidazole structure for selective anion separation. ACS Nano. 2022;16(3):4629–41.
93. Zheng X, Song Y, Liu Y, Li J, Yang Y, Wu D, et al. Synthesis of phase junction cadmium sulfide photocatalyst under sulfur-rich solution system for efficient photocatalytic hydrogen evolution. Small. 2023;19:2207623.
94. Yong Z, Yap L, Shi Q, Chesman A, Chen E, Fu R, et al. Omnidirectional hydrogen generation based on a flexible black gold nanotube array. ACS Nano. 2022;16:14963–72.
95. Tseng W, Rau J, Chiou H, Tseng W. Synthesis of gold nanoclusters-loaded lysozyme nanoparticles for ratiometric fluorescent detection of cyanide in tap water, cyanogenic glycoside-containing plants, and soils. Environ Res. 2022;207: 112144.
96. Wang J, Qiu Y, Li D, Liu X, Jiang C, Huang L, et al. Ratiometric fluorometric and visual determination of cyanide based on the use of carbon dots and gold nanoclusters. Mikrochim Acta. 2019;186:809.
97. Wang W, Kong Y, Jiang J, Xie Q, Huang Y, Li G, et al. Engineering the protein corona structure on gold nanoclusters enables red-shifted emissions in the second near-infrared window for gastrointestinal imaging. Angew Chem Int Ed. 2020;59(50):22431–5.
98. Yang H, Yang Y, Liu S, Zhan X, Zhou H, Li X, et al. Ratiometric and sensitive cyanide sensing using dual-emissive gold nanoclusters. Anal Bioanal Chem. 2020;412(23):5819–26.
99. Xiang H, He S, Zhao G, Zhang M, Lin J, Yang L, et al. Gold nanocluster-based ratiometric probe with surface structure regulation-triggered sensing of hydrogen sulfide in living organisms. Acs Appl Mater Inter. 2023;15(10):12643–52.
100. Yan L, Gu Q, Jiang W, Tan M, Tan Z, Mao G, et al. Near-infrared fluorescent probe with large stokes shift for imaging of hydrogen sulfide in tumor-bearing mice. Anal Chem. 2022;94(14):5514–20.
101. Singh N, Sharma S, Singh R, Rajput S, Chattopadhyay N, Tewari D, et al. A naphthalimide-based peptide conjugate for concurrent imaging and apoptosis induction in cancer cells by utilizing endogenous hydrogen sulfide. Chem Sci. 2021;12(48):16085–91.
102. Duan C, Won M, Verwilst P, Xu J, Kim H, Zeng L, et al. In vivo imaging of endogenously produced HCLO in zebrafish and mice using a bright, photostable ratiometric fluorescent probe. Anal Chem. 2019;91(6):4172–8.
103. Zuo M, Duan Q, Li C, Ge J, Wang Q, Li Z, et al. A versatile strategy for constructing ratiometric upconversion luminescent probe with sensitized emission of energy acceptor. Anal Chem. 2021;93(13):5635–43.
104. Yu Y, Li G, Wu D, Zheng F, Zhang X, Liu J, et al. Determination of hydrogen sulfide in wines based on chemical-derivatization-triggered aggregation-induced emission by high-performance liquid chromatography with fluorescence detection. J Agr Food Chem. 2020;68(3):876–83.
105. Xu T, Scafa N, Xu L, Zhou S, Al-Ghanem K, Mahboob S, et al. Electrochemical hydrogen sulfide biosensors. Analyst. 2016;141(4):1185–95.
106. Qin Z, Su W, Liu P, Ma J, Zhang Y, Jiao T. Facile preparation of a rhodamine B derivative-based fluorescent probe for visual detection of iron ions. ACS Omega. 2021;6(38):25040–8.
107. Amiri M, Salehniya H, Habibi-Yangjeh A. Graphitic carbon nitride/chitosan composite for adsorption and electrochemical determination of mercury in real samples. Ind Eng Chem Res. 2016;55(29):8114–22.
108. Janani B, Syed A, Thomas AM, Bahkali AH, Elgorban AM, Raju LL, et al. UV–vis spectroscopic method for the sensitive and selective detection of mercury by silver nanoparticles in presence of alanine. Optik. 2020;204: 164160.
109. Khoshbin Z, Housaindokht MR, Verdian A, Bozorgmehr MR. Simultaneous detection and determination of mercury (II) and lead (II) ions through the achievement of novel functional nucleic acid-based biosensors. Biosens Bioelectron. 2018;116:130–47.
110. Liu J, Wu D, Yan X, Guan Y. Naked-eye sensor for rapid determination of mercury ion. Talanta. 2013;116:563–8.
111. Narayanan KB, Han SS. Highly selective and quantitative colorimetric detection of mercury(II) ions by carrageenan-functionalized Ag/AgCl nanoparticles. Carbohydr Polym. 2017;160:90–6.
112. Omer KM, Hama Aziz KH, Mohammed SJ. Improvement of selectivity via the surface modification of carbon nanodots towards the quantitative detection of mercury ions. New J Chem. 2019;43(33):12979–86.
113. Liu W, Wang X, Wang Y, Li J, Shen D, Kang Q, et al. Ratiometric fluorescence sensor based on dithiothreitol modified carbon dots-gold nanoclusters for the sensitive detection of mercury ions in water samples. Sens Actuators B Chem. 2018;262:810–7.
114. Lee J, Park J, Hee Lee H, Park H, Kim HI, Kim WJ. Fluorescence switch for silver ion detection utilizing dimerization of DNA-Ag nanoclusters. Biosens Bioelectron. 2015;68:642–7.
115. Kim JH, Kim KB, Park JS, Min N. Single cytosine-based electrochemical biosensor for low-cost detection of silver ions. Sens Actuators B Chem. 2017;245:741–6.
116. Long Q, Wen Y, Li H, Zhang Y, Yao S. A novel fluorescent biosensor for detection of silver ions based on upconversion nanoparticles. J Fluoresc. 2017;27(1):205–11.
117. Saleh SM, Almotiri MK, Ali R. Green synthesis of highly luminescent gold nanoclusters and their application in sensing Cu(II) and Hg(II). J Photochem. 2022;426: 113719.
118. Zhang Y, Jiang H, Wang X. Cytidine-stabilized gold nanocluster as a fluorescence turn-on and turn-off probe for dual functional detection of Ag(+) and Hg(2+). Anal Chim Acta. 2015;870:1–7.
119. Jiang H, Zhang Y, Wang X. Single cytidine units-templated syntheses of multicolored water-soluble Au nanoclusters. Nanoscale. 2014;6(17):10355–62.
120. Dai H, Shi Y, Wang Y, Sun Y, Hu J, Ni P, et al. Label-free turn-on fluorescent detection of melamine based on the anti-quenching ability of Hg^{2+} to gold nanoclusters. Biosens Bioelectron. 2014;53:76–81.
121. Mu X, Qi L, Dong P, Qiao J, Hou J, Nie Z, et al. Facile one-pot synthesis of L-proline-stabilized fluorescent gold nanoclusters

and its application as sensing probes for serum iron. Biosens Bioelectron. 2013;49:249–55.
122. Wang R, Wang W, Ren H, Chae J. Detection of copper ions in drinking water using the competitive adsorption of proteins. Biosens Bioelectron. 2014;57:179–85.
123. Khan I, Niazi S, Yu Y, Pasha I, Yue L, Mohsin A, et al. Fabrication of PAA coated green-emitting AuNCs for construction of label -free FRET assembly for specific recognition of T-2 toxin. Sens Actuators B Chem. 2020;321: 128470.
124. Kalinowska M, Sienkiewicz-Gromiuk J, Swiderski G, Pietryczuk A, Cudowski A, Lewandowski W. Zn(II) complex of plant phenolic chlorogenic acid: antioxidant, antimicrobial and structural studies. Materials. 2020;13:3745.
125. Ali R, Saleh S, Aly S. Fluorescent gold nanoclusters as pH sensors for the pH 5 to 9 range and for imaging of blood cell pH values. Mikrochim Acta. 2017;184(9):3309–15.
126. Desai ML, Basu H, Saha S, Singhal RK, Kailasa SK. One pot synthesis of fluorescent gold nanoclusters from extract for independent detection of Cd^{2+}, Zn^{2+} and Cu^{2+} ions with high sensitivity. J Mol Liq. 2020;304: 112697.
127. Gong M, Dai H. A mini review of NiFe-based materials as highly active oxygen evolution reaction electrocatalysts. Nano Res. 2014;8(1):23–39.
128. Tang C, Asirib AM, Sun XP. Highly-active oxygen evolution electrocatalyzed by a Fe-doped NiSe nanoflake array electrode. Chem Comm. 2016;52(24):4529–32.
129. Zamojc K, Zdrowowicz M, Rudnicki-Velasquez PB, Krzyminski K, Zaborowski B, Niedzialkowski P, et al. The development of 1,3-diphenylisobenzofuran as a highly selective probe for the detection and quantitative determination of hydrogen peroxide. Free Radic Res. 2017;51(1):38–46.
130. Dong W, Sun C, Sun M, Ge H, Asiri A, Marwani H, et al. Fluorescent copper nanoclusters for the iodide-enhanced detection of hypochlorous acid. Acs Appl Nano Mater. 2020;3(1):312–8.
131. Quan Z, Xue F, Li H, Chen Z, Wang L, Zhu H, et al. A bioinspired ratiometric fluorescence probe based on cellulose nanocrystal-stabilized gold nanoclusters for live-cell and zebrafish imaging of highly reactive oxygen species. Chem Eng J. 2022;431: 133954.
132. Chen T, Hu Y, Cen Y, Chu X, Lu Y. A dual-emission fluorescent nanocomplex of gold-cluster-decorated silica particles for live cell imaging of highly reactive oxygen species. J Am Chem Soc. 2013;135(31):11595–602.
133. Li P, Lin J, Chen C, Ciou W, Chan P, Luo L, et al. Using gold nanoclusters as selective luminescent probes for phosphate-containing metabolites. Anal Chem. 2012;84(13):5484–8.
134. Wei H, Wang Z, Zhang J, House S, Gao Y, Yang L, et al. Time-dependent, protein-directed growth of gold nanoparticles within a single crystal of lysozyme. Nat Nanotechnol. 2011;6(2):93–7.
135. Si D, Epstein T, Lee Y, Kopelman R. Nanoparticle PEBBLE sensors for quantitative nanomolar imaging of intracellular free calcium ions. Anal Chem. 2012;84(2):978–86.
136. Medley C, Bamrungsap S, Tan W, Smith J. Aptamer-conjugated nanoparticles for cancer cell detection. Anal Chem. 2011;83(3):727–34.
137. Lee J, Lee N, Kim H, Kim J, Choi S, Kim J, et al. Uniform mesoporous dye-doped silica nanoparticles decorated with multiple magnetite nanocrystals for simultaneous enhanced magnetic resonance imaging, fluorescence imaging, and drug delivery. J Am Chem Soc. 2010;132(2):552–7.
138. Elsabahy M, Wooley K. Design of polymeric nanoparticles for biomedical delivery applications. Chem Soc Rev. 2012;41(7):2545–61.
139. Yu M, Zhou C, Liu J, Hankins J, Zheng J. Luminescent gold nanoparticles with pH-dependent membrane adsorption. J Am Chem Soc. 2011;133(29):11014–7.
140. Chen C, Zhou L, Liu W, Liu W. Coumarinocoumarin-based two-photon fluorescent cysteine biosensor for targeting lysosome. Anal Chem. 2018;90(10):6138–43.
141. Liu L, Zhu G, Zeng W, Yi Y, Lv B, Qian J, et al. Silicon quantum dot-coated onto gold nanoparticles as an optical probe for colorimetric and fluorometric determination of cysteine. Mikrochim Acta. 2019;186(2):98.
142. McConnell E, Smythers A, Hicks L. Maleimide-based chemical proteomics for quantitative analysis of cysteine reactivity. J Am Soc Mass Spectr. 2020;31(8):1697–705.
143. Zhao Y-H, Luo Y, Wang H, Guo T, Zhou H, Tan H, et al. A new fluorescent probe based on aggregation induced emission for selective and quantitative determination of copper(ii) and its further application to cysteine detection. ChemistrySelect. 2018;3(5):1521–6.
144. Yu X, Zhang C, Zhang L, Xue Y, Li H, Wu Y. The construction of a FRET assembly by using gold nanoclusters and carbon dots and their application as a ratiometric probe for cysteine detection. Sensor Actuat B-Chem. 2018;263:327–35.
145. Okamoto K, Sako Y. Recent advances in FRET for the study of protein interactions and dynamics. Curr Opin Struc Biol. 2017;46:16–23.
146. Ding H, Yu S, Wei J, Xiong H. Full-color light-emitting carbon dots with a surface-state-controlled luminescence mechanism. ACS Nano. 2016;10(1):484–91.
147. Hola K, Zhang Y, Wang Y, Giannelis E, Zboril R, Rogach A. Carbon dots-emerging light emitters for bioimaging, cancer therapy and optoelectronics. Nano Today. 2014;9(5):590–603.
148. Liu J, Duchesne P, Yu M, Jiang X, Ning X, Vinluan R, et al. Luminescent gold nanoparticles with size-independent emission. Angew Chem Int Ed. 2016;55(31):8894–8.
149. Wang M, Zhang J, Zhou X, Sun H, Su X. Fluorescence sensing strategy for xanthine assay based on gold nanoclusters and nanozyme. Sens Actuators B Chem. 2022;358: 131488.
150. Govindaraju S, Ankireddy SR, Viswanath B, Kim J, Yun K. Fluorescent gold nanoclusters for selective detection of dopamine in cerebrospinal fluid. Sci Rep. 2017;7:40298.
151. Li Q, Zhou X, Tan L, Shang L. MOF-based surface tailoring the near-infrared luminescence property of gold nanoclusters for ratiometric fluorescence sensing of acetylcholinesterase. Sens Actuators B Chem. 2023;385: 133695.
152. You JG, Lu CY, Krishna Kumar AS, Tseng WL. Cerium(iii)-directed assembly of glutathione-capped gold nanoclusters for sensing and imaging of alkaline phosphatase-mediated hydrolysis of adenosine triphosphate. Nanoscale. 2018;10(37):17691–8.
153. Feng X, Cao Y, Ding Y, Zheng H. Development and validation for the quantitative determination of xanthine oxidoreductase inhibitor topiroxostat by LC-MS/MS and its clinico-pharmacokinetic study. J Pharm Biomed Anal. 2020;189: 113470.
154. Yang H, Li X, Li G, Huang H, Yang W, Jiang X, et al. Accurate quantitative determination of affinity and binding kinetics for tight binding inhibition of xanthine oxidase. Biomed Pharmacother. 2021;139: 111664.
155. Wang J, Ni P, Chen C, Jiang Y, Zhang C, Wang B, et al. Colorimetric determination of the activity of alkaline phosphatase by exploiting the oxidase-like activity of palladium cube@CeO2 core-shell nanoparticles. Mikrochim Acta. 2020;187(2):115.
156. Wang S, Huang M, Hua J, Wei L, Lin S, Xiao L. Digital counting of single semiconducting polymer nanoparticles for the detection of alkaline phosphatase. Nanoscale. 2021;13(9):4946–55.
157. Wang XX, Wu Q, Shan Z, Huang QM. BSA-stabilized Au clusters as peroxidase mimetics for use in xanthine detection. Biosens Bioelectron. 2011;26(8):3614–9.
158. Jin L, Shang L, Guo S, Fang Y, Wen D, Wang L, et al. Biomolecule-stabilized Au nanoclusters as a fluorescence probe for sensitive detection of glucose. Biosens Bioelectron. 2011;26(5):1965–9.

159. Liu Y, Ai K, Cheng X, Huo L, Lu L. Gold-nanocluster-based fluorescent sensors for highly sensitive and selective detection of cyanide in water. Adv Funct. 2010;20(6):951–6.
160. Liu H, Li M, Xia Y, Ren X. A Turn-on fluorescent sensor for selective and sensitive detection of alkaline phosphatase activity with gold nanoclusters based on inner filter effect. ACS Appl Mater Interfaces. 2017;9(1):120–6.
161. Zhang H, Xu C, Liu J, Li X, Guo L, Li X. An enzyme-activatable probe with a self-immolative linker for rapid and sensitive alkaline phosphatase detection and cell imaging through a cascade reaction. ChemComm. 2015;51(32):7031–4.
162. Liu S, Pang S, Na W, Su X. Near-infrared fluorescence probe for the determination of alkaline phosphatase. Biosens Bioelectron. 2014;55:249–54.
163. Li G, Fu H, Chen X, Gong P, Chen G, Xia L, et al. Facile and sensitive fluorescence sensing of alkaline phosphatase activity with photoluminescent carbon dots based on inner filter effect. Anal Chem. 2016;88(5):2720–6.
164. Chang H, Ho JA. Gold nanocluster-assisted fluorescent detection for hydrogen peroxide and cholesterol based on the inner filter effect of gold nanoparticles. Anal Chem. 2015;87(20):10362–7.
165. Yan X, Li H, Han X, Su X. A ratiometric fluorescent quantum dots based biosensor for organophosphorus pesticides detection by inner-filter effect. Biosens Bioelectron. 2015;74:277–83.
166. Kurdekar A, Chunduri L, Chelli S, Haleyurgirisetty M, Bulagonda E, Zheng J, et al. Fluorescent silver nanoparticle based highly sensitive immunoassay for early detection of HIV infection. RSC Adv. 2017;7(32):19863–77.
167. He Q, Zhu Z, Jin L, Peng L, Guo W, Hu S. Detection of HIV-1 p24 antigen using streptavidin-biotin and gold nanoparticles based immunoassay by inductively coupled plasma mass spectrometry. J Anal At Spectrom. 2014;29(8):1477–82.
168. Kurdekar AD, Avinash Chunduri LA, Manohar CS, Haleyurgirisetty MK, Hewlett IK, Venkataramaniah K. Streptavidin-conjugated gold nanoclusters as ultrasensitive fluorescent sensors for early diagnosis of HIV infection. Sci Adv. 2018;4(11):eaar6280.
169. Chunduri L, Haleyurgirisetty M, Patnaik S, Bulagonda P, Kurdekar A, Liu J, et al. Development of carbon dot based microplate and microfluidic chip immunoassay for rapid and sensitive detection of HIV-1 p24 antigen. Microfluid Nanofluidics. 2016;20(12):167.
170. Chunduri L, Kurdekar A, Haleyurgirisetty M, Bulagonda E, Kamisetti V, Hewlett I. Femtogram level sensitivity achieved by surface engineered silica nanoparticles in the early detection of hiv infection. Sci Rep. 2017;7:7149.
171. Liu J, Du B, Zhang P, Haleyurgirisetty M, Zhao J, Ragupathy V, et al. Development of a microchip europium nanoparticle immunoassay for sensitive point-of-care HIV detection. Biosens Bioelectron. 2014;61:177–83.
172. Kurdekar A, Chunduri LA, Bulagonda E, Haleyurgirisetty M, Kamisetti V, Hewlett I. Comparative performance evaluation of carbon dot-based paper immunoassay on Whatman filter paper and nitrocellulose paper in the detection of HIV infection. Microfluid Nanofluidics. 2016;20(7):99.
173. Shi WQ, Zeng LL, He RL, Han XS, Guan ZJ, Zhou M, et al. Near-unity NIR phosphorescent quantum yield from a room-temperature solvated metal nanocluster. Science. 2024;383:326–30.
174. Huang J, Xie C, Zhang X, Jiang Y, Li J, Fan Q, et al. Renal-clearable molecular semiconductor for second near-infrared fluorescence imaging of kidney dysfunction. Angew Chem Int Edit. 2019;58(42):15120–7.
175. Ma H, Wang J, Zhang X-D. Near-infrared II emissive metal clusters: from atom physics to biomedicine. Coord Chem Rev. 2021;448: 214184.
176. Liu L, Mu X, Liu H, Wang Q, Bai X, Wang J, et al. Structure, luminescence, and bioimaging of bimetallic CuAu nanoclusters. Opt Mater. 2018;86:291–7.
177. Liu S, Zhang XD, Gu X, Ming D. Photodetectors based on two dimensional materials for biomedical application. Biosens Bioelectron. 2019;143: 111617.
178. Hegde M, Pai P, Shetty MG, Babitha KS. Gold nanoparticle based biosensors for rapid pathogen detection: a review. Environ Nanotechnol Monit Manag. 2022;18: 100756.
179. Ma Z, Wan H, Wang W, Zhang X, Uno T, Yang Q, et al. A theranostic agent for cancer therapy and imaging in the second near-infrared window. Nano Res. 2019;12:273–9.
180. Mu X, Wang J, Li Y, Xu F, Long W, Ouyang L, et al. Redox trimetallic nanozyme with neutral environment preference for brain injury. ACS Nano. 2019;13(2):1870–84.
181. Pei J, Zhao R, Mu X, Wang J, Liu C, Zhang XD. Single-atom nanozymes for biological applications. Biomater Sci. 2020;8(23):6428–41.
182. Qiao Y, Liu Y, Liu H, Li Y, Long W, Wang J, et al. Fluorescence enhancement of gold nanoclusters via Zn doping for biomedical applications. RSC Adv. 2018;8(14):7396–402.
183. Ren Q, Sun S, Zhang X-D. Redox-active nanoparticles for inflammatory bowel disease. Nano Res. 2021;14(8):2535–57.
184. Wan H, Yue J, Zhu S, Uno T, Zhang X, Yang Q, et al. A bright organic NIR-II nanofluorophore for three-dimensional imaging into biological tissues. Nat Commun. 2018;9(1):2041–1723.
185. Wei D, Yu Y, Huang Y, Jiang Y, Zhao Y, Nie Z, et al. A near-infrared-II polymer with tandem fluorophores demonstrates superior biodegradability for simultaneous drug tracking and treatment efficacy feedback. ACS Nano. 2021;15(3):5428–38.
186. Yan R, Sun S, Yang J, Long W, Wang J, Mu X, et al. nanozyme-based bandage with single-atom catalysis for brain trauma. ACS Nano. 2019;13(10):11552–60.